TURUN YLIOPISTO
UNIVERSITY OF TURKU

LOW BANDWIDTH MANGANITE (Gd, Ca)MnO_3 FOR FUTURE MEMRISTOR DEVICES

Azar Beiranvand

TURUN YLIOPISTON JULKAISUJA – ANNALES UNIVERSITATIS TURKUENSIS
SARJA – SER. AI OSA – TOM. 669 | ASTRONOMICA – CHEMICA – PHYSICA – MATHEMATICA | TURKU 2022

TURUN YLIOPISTO
UNIVERSITY OF TURKU

LOW BANDWIDTH MANGANITE (Gd, Ca)MnO_3 FOR FUTURE MEMRISTOR DEVICES

Azar Beiranvand

TURUN YLIOPISTON JULKAISUJA – ANNALES UNIVERSITATIS TURKUENSIS
SARJA – SER. AI OSA – TOM. 669 | ASTRONOMICA – CHEMICA – PHYSICA – MATHEMATICA | TURKU 2022

University of Turku

Faculty of Science
Department of Physics and Astronomy
Physics
Doctoral programme in Exact Sciences

Supervised by

Professor, Petriina Paturi
Wihuri Physical Laboratory
Department of Physics and Astronomy
University of Turku, Finland

Dr., Hannu Huhtinen
Wihuri Physical Laboratory
Department of Physics and Astronomy
University of Turku, Finland

Reviewed by

Ass. prof., Tapati Sarkar
Division of Solid State Physics
Department of Materials Science and Engineering
Uppsala University, Sweden

Dr., Otto Mustonen
School of Chemistry
University of Birmingham, United Kingdom

Opponent

Professor, Mogens Christensen
Centre for Integrated Materials Research (iMAT)
Department of Chemistry and iNANO
Århus University, Denmark

ISBN 978-951-29-8864-8 (PRINT)
ISBN 978-951-29-8865-5 (PDF)
ISSN 0082-7002 (Print)
ISSN 2343-3175 (Online)
Painosalama, Turku, Finland 2022

This book is dedicated to my beloved husband Amin
and my sweetheart daughter Anahita

UNIVERSITY OF TURKU
Faculty of Science
Department of Physics and Astronomy
Physics
BEIRANVAND, AZAR: LOW BANDWIDTH MANGANITE (Gd, Ca)MnO_3 FOR FUTURE MEMRISTOR DEVICES
Doctoral dissertation, 116 pp.
Doctoral programme in Exact Sciences
May 2022

ABSTRACT

In this thesis, the magnetic phase diagram of $Gd_{1-x}Ca_xMnO_3$ $0\leq x \leq 1$ (here after GCMO) was constructed and described based on the magnetic and resistivity measurements. This compound with perovskite structure belongs to low bandwidth manganites, which are famous for having colossal magnetoresistance properties. The introduction begins with description of the basic structural and typical magnetic interactions, which explain the magnetic and magneto-transport properties in manganites. Also, the fundamental physics relevant to this work is widely discussed.

The experimental research was based on synthesis and characterisation of GCMO compound in forms of polycrystalline bulk and thin film. The GCMO polycrystalline samples were synthesized by a conventional solid state method. The thin films were fabricated by pulsed laser deposition (PLD). The structural characterisation of the samples was done using x-ray diffraction and the magnetic and magnetoresistive properties were investigated by SQUID magnetometry and magneto-transport measurements down to the liquid helium temperature.

The properties of the polycrystalline samples were determined at different Ca doping levels. In the region of $0.5\leq x \leq 0.7$, the samples, albeit they are antiferromagnetic insulators (AFMI), show charge ordering state near the room temperature, which cause the high conductivity at this temperature range. However, only in electron doped region, $x = 0.9$, the sample shows magnetoresistance properties, where the ferromagnetic phase is arrested within the antiferromagnetic matrix. Based on these results and in comparison with phase diagrams of other low bandwidth manganites, $Sm_{1-x}Ca_xMnO_3$ (SCMO) and $Pr_{1-x}Ca_xMnO_3$ (PCMO), the magnetic phase diagram was established for polycrystalline GCMO compounds.

The influence of substrate materials was explored in structural, magnetic and electrical properties of the epitaxially grown GCMO thin films. We show that how the lattice mismatch between the selected substrate and the GCMO film can affect on crystal domain orientation and the substrate-film interface properties, consequently affecting the magnetic and electrical properties of the film. These results give us an outline to choose the optimal substrate, i.e. $SrTiO_3$ (STO) for the GCMO compounds. In addition, the magnetic phase diagram of the GCMO thin films deposited on STO substrate is produced based on magnetic transitions and it is compared with the phase diagram of the polycrystalline bulk, where the differences and similarities are widely discussed.

Finally, two Ca concentrations, x = 0.4 and x = 0.9, were selected to investigate the effect of *in situ* vacuum and oxygen treatments. The results demonstrate that the vacuum annealing induced more oxygen vacancies and oxygen vacancy complexes in the GCMO lattice when compared with the pristine film for both concentrations. In contrast, after oxygen treatment, the films contain smaller amount of oxygen vacancies and oxygen vacancy complexes in their lattice. However, both treatments increase the density of defects in the film-substrate interface and on the surface of the film, improving the magnetoresistive properties, which make the GCMO thin film as good candidate for future memristor applications.

TURUN YLIOPISTO
Matemaattis-luonnontieteellinen tiedekunta
Fysiikan ja tähtitieteen laitos
Fysiikka
BEIRANVAND, AZAR: LOW BANDWIDTH MANGANITE (Gd, Ca)MnO_3 FOR FUTURE MEMRISTOR DEVICES
Väitöskirja, 116 s.
Eksaktien tieteiden tohtoriohjelma
Toukokuu 2022

TIIVISTELMÄ

Tämä väitöskirjatyö liittyy kokeellisen materiaalitutkimuksen alaan ja se käsittää tulevaisuuden spintroniikan kannalta mielenkiintoisen perovskiittirakenteisen $\mathrm{Gd}_{1-x}\mathrm{Ca}_x\mathrm{MnO}_3$ (GCMO)-manganiitin rakenteellisia, magneettisia ja sähköisiä tutkimuksia. Tutkimuksissa pystyttiin dooppauskonsentraation funktiona muodostamaan materiaalin faasiadiagrammit sekä monikiteisille jauhenäytteille että sovellusten kannalta oleellisille ohutkalvoille, ja nämä tuottivat uutta tietoa materiaalin magneettisista ominaisuuksista laajalla lämpötila-alueella. Väitöskirjatyön keskeiset tulokset osoittavat GCMO-ohutkalvojen toimivan myös memristoreina, joita voidaan hyödyntää tulevaisuuden neuromorfisissa sovelluksissa.

Väitöskirja jakautuu kolmeen pääosaan: johdantoon, käytettyjen tutkimusmenetelmien esittelyyn sekä tulosten esittämiseen ja niiden analysointiin. Alun johdanto-osassa käsitellään käytettyjen materiaalien perusominaisuuksia, keskittyen syvällisemmin manganiiteissa esiintyviin magneettisiin vuorovaikutuksiin sekä esitellään malleja, jotka kuvaavat materiaalien magneettisia ja sähköisiä ominaisuuksia. Tutkimusmenetelmäosassa esitellään materiaalien valmistuksessa sekä tutkimuksissa käytetyt metodit. Nämä pitävät sisällään keraamisen materiaalin syntetisoinnin kiinteän aineen reaktiolla ja ohutkalvojen valmistuksen laserhöyrystyksellä sekä materiaalien rakenteeellisiin karakterisointeihin käytetyt menetelmät kuten röntgendiffraktion, röntgenheijastuksen, läpivalaisuelektronimikroskopian, fotoelektronispektroskopian ja positroniannihilaatiospektroskopian. Myös keraamisten materiaalien ja ohutkalvojen tutkimuksissa käytetyt menetelmät kuten laajalla lämpötila- ja magneettikenttäalueilla tehdyt magneettiset ja sähköiset tutkimusmenetelmät esitellään pääpiirteissään.

Työn kokeellinen osuus on jaettu kahteen osaan, joissa monikiteisten GCMO-keraamien sekä toisaalta niistä valmistettujen ohutkalvojen ominaisuudet on esitetty uusimpien tutkimustulosten valossa. Perustutkimuksellisesti merkittävintä on se, että näiden ominaisuudet on ensimmäistä kertaa kartoitettu dooppaamalla Ca:lla GCMO:n perovskiittirakenteessa olevaa Gd:a. Tutkimusten perusteella tulokset on jaettu kolmeen pääluokkaan, jossa dooppausasteella $x \leq 0.4$, $0.5 \leq x \leq 0.7$ ja $x \geq 0.8$ havaittiin olevan suuria eroja materiaalin magneettisissa ja magnetoresistiivisissä ominaisuuksissa. Sovellusten näkökulmasta tärkeiden ohutkalvojen ominaisuudet optimoitiin myös erilaisten kasvatusalustojen ja lämpökäsittelyjen tapauksissa. Yhdistelemällä lopulta kaikkien väitöskirjassa olevien osajulkaisujen tulokset, pystyttiin päättelemään optimaaliset dooppauskonsentraatiot, alustamateriaalit sekä toisaalta valmistusparametrit

sellaisille ohutkalvoille, jotka voisivat toimia perusyksikköina tulevaisuuden spintroniikassa ja erilaisissa muistisovellusratkaisuissa.

Acknowledgements

This work has been carried out in the Wihuri Physical Laboratory of the Department of Physics and Astronomy at the University of Turku. The Väisälä Foundation, Finnish Cultural Foundation, Jenny and Antti Wihuri Foundation and the University of Turku Graduate School's Doctoral Programme in Physical and Chemical Sciences are acknowledged for their financial support. I'm thankful to Ass. prof. Tapati Sarkar and Dr. Otto Mustonen for their insightful reviewing of this dissertation. I also would like to thank Professor Mogens Christensen, it is a great honor to have you as my opponent. I dedicate my deepest gratitude to Prof. Petriina Paturi, not only for her effective supervision, constructive advise and comments and her commitment to the whole group but also for her personal trust, kindness and all financial supports, which made this thesis possible. Furthermore, I would like to thank Dr. Hannu Huhtinen who taught me working with PLD and magnetometer, revised my manuscripts and writings, and made the atmosphere of the Wihuri Physical Laboratory friendly. Special thanks goes to Dr. Jussi Tikkanen from whom I leaned materials synthesis and XRD measurements. I also want to thank the all my colleagues in our research group. I would like to thank my parents and my sisters for their love, caring and support in all my life. I wish to have thanks to my family especially my dear husband, Amin who has always pushed me to follow my dreams and encouraged me to go forward even in hard times. Thanks for your love, company and invaluable support, none of these would have been possible without you. Finally, I wish to thank my sweetheart daughter, Anahita who makes my life meaningful, enjoyable and beautiful. Having you is the best thing that ever happened to me.

April 2022
Azar Beiranvand

Table of Contents

Abbreviations

GCMO	$Gd_{1-x}Ca_xMnO_3$
FM	Ferromagnetic
AFM	Antiferromagnetic
FMM	Ferromagnetic metallic
AFMI	Antiferromagnetic insulator
CGI	Cluster glass insulator
CO/OO	Charge ordering/orbital ordering
IMT	Insulator-to-metal transition
SE	Superexchange
DE	Double exchange
JT	Jahn-Teller
MCE	Magnetocaloric effect
RT	Room temperature
T_C	Curie temperature
T_{CO}	Charge ordering temperature
B_c	Coercive force
R	Resistance
MR	Magnetoresistance
CMR	Colossal magnetoresistance
STO	$SrTiO_3$
SLAO	$SrLaAlO_3$
LSAT	$(LaAlO_3)_{0.3}(Sr_2AlTaO_6)_{0.7}$
XRD	X-ray diffraction
XRR	X-ray reflection
XPS	X-ray photoelectron spectroscopy
TEM	Transmission electron microscopy
HRTEM	High resolution transmission electron microscopy
FFT	Fast Fourier transform
RMS	Root mean square of a surface roughness
PPMS	Physical property measurement system
SQUID	Superconducting quantum interference device
PAS	Positron annihilation spectroscopy
PALS	Positron annihilation lifetime spectroscopy

List of Original Publications

This dissertation is based on the following original publications, which are referred to in the text:

I A. Beiranvand, J. Tikkanen, H. Huhtinen and P. Paturi. Electronic and magnetic phase diagram of polycrystalline $Gd_{1-x}Ca_xMnO_3$ manganites. Journal of Alloys and Compounds, 2017; 720: 126–130.

II A. Beiranvand, J. Tikkanen, J. Rautakoski, H. Huhtinen and P. Paturi. Estimates of the magnetocaloric effect in (Nd, Ca)MnO_3 and (Gd, Ca)MnO_3 based on magnetic transition entropies. Journal of Materials Research Express, 2017; 4: 036101–036113.

III A. Beiranvand, E. Rivasto, H. Huhtinen and P. Paturi. Strain induced domain structure and its impact on magnetic and transport properties of $Gd_{0.6}Ca_{0.4}MnO_3$ thin films. ACS Omega, 2021; 6:34572–34579.

IV A. Beiranvand, J. Tikkanen, H. Huhtinen and P. Paturi. Metamagnetic transition and spin memory effect in epitaxial $Gd_{1-x}Ca_xMnO_3$ ($0\leq x \leq 1$) thin films. Journal of Magnetism and Magnetic Materials, 2019; 469: 253–258.

V A. Beiranvand, M. O. Liedke, C. Haalisto, V. Lähteenlahti, A. Schulman, S. Granroth, H. Palonen, M. Butterling, A. Wagner, H. Huhtinen and P. Paturi. Tuned AFM-FM coupling by the formation of vacancy complex in $Gd_{0.6}Ca_{0.4}MnO_3$ thin film lattice. Journal of Physics: Condensed Matter, 2021; 33: 255803–255812.

VI A. Beiranvand, M. O. Liedke, C. Haalisto, V. Lähteenlahti, A. Schulman, S. Granroth, H. Palonen, M. Butterling, A. Wagner, H. Huhtinen and P. Paturi. Manipulating magnetic and magnetoresistive properties by oxygen vacancy complexes in $Gd_{0.1}Ca_{0.9}MnO_3$ thin films. Journal of Physics: Condensed Matter, 2022; 34: 155804:1–10.

Articles relevant to this work but not included in this thesis

VII A. Schulman, A. Beiranvand, V. Lähteenlahti, H. Huhtinen and P. Paturi. Appearance of glassy ferromagnetic behavior in $Gd_{1-x}Ca_xMnO_3$ ($0 \leq x \leq 1$) thin films: A revised phase diagram. Journal of Magnetism and Magnetic Materials, 2020; 498: 166149:1–6.

VIII V. Lähteenlahti, A. Schulman, A. Beiranvand, H. Huhtinen, P. Paturi. Electron doping effect in the resistive switching properties of Al/$Gd_{1-x}Ca_xMnO_3$/Au memristor devices. ACS Applied Materials and Interfaces, 2021; 13: 18365–18371.

IX A. Schulman, H. Palonen, V. Lähteenlahti, A. Beiranvand, H. Huhtinen and P. Paturi. Metastable ferromagnetic flux closure-type domains in strain relaxed $Gd_{0.1}Ca_{0.9}MnO_3$ thin films. Journal of Physics: Condensed Matter, 2021; 33: 035803: 1–7.

1 Motivation

The main component of the neuromorphic computer is an adaptive element that has a multiply-valued internal state that can be tuned in a non-volatile or quasi-stable manner. The particular internal state can be e.g. resistivity, permittivity, polarization, magnetization or optical transmission. The simplest of these adaptive electronics elements is the memristor (also resistive random access memory, RAM), a resistance element that has memory. The most common memristors have a capacitor like structure, where the material between the electrodes is typically a transition metal oxide or a perovskite oxide [1].

In perovskite manganite memristors (almost singularly $Pr_{0.7}Ca_{0.3}MnO_3$, PCMO-0.3), the most probable working principle is migration of oxygen near the Schottky interface between the non-noble metal electrode and the manganite. Oxygen migration from the PCMO to the electrode leads to the oxidation of the metal and the high resistance state. An opposite voltage reverses the oxygen migration and reduces the memristor back to the low resistance state [2].

In Mott insulator-to-metal transition (IMT), the electrons localized at individual atoms are released to the conduction band by some outside incentive, such as electric field, magnetic field, pressure or illumination. The effect is due to the correlation effects between the electrons in the material. Mott IMT is a first order phase transition enabling metastable ”superheated” or ”supercooled” states. This leads to desired memory effect. To work as a Mott memristor, the oxide layer needs to have an insulating or semiconducting room temperature localized electron state, which can then melt to the metallic state under the electric field. The IMT should also allow metastable states.

In the perovskite structured manganites, the low one electron bandwidth (W) compositions, $Ln_{1-x}Ca_xMnO_3$ with Ln = Pr, Sm or Gd have a charge and orbital ordered state (CO/OO) close to the room temperature. The CO-state is visible as a peak in the magnetization curve below which the zero field and field cooled $M(T)$-curves diverge. The charge ordering temperature generally increases as the size of the lanthanide atom decreases (La $\rightarrow$ Gd) and the structural tolerance factor decreases. Structurally this is because the MnO_6 octahedra tilt more to accommodate the small lanthanide atom. In the IMT, the used electric field delocalizes the electrons by dynamically reducing the chequerboard Jahn-Teller distortion of the octahedra. The induced transition is of the first order and thus can be ”supercooled” or ”superheated”. The metastable low resistance state can be switched back to the stable state with an opposite electric field. This leads to the desired memory effect. In the literature, only PCMO-0.3 memristors have been systematically reported so far, and it has been shown to rely on interface oxygen vacancies [2]. The more promising Sm- and Gd-based memristors have not been studied prior to this work.

In this work, in the first part, the magnetic phase diagram of $Gd_{1-x}Ca_xMnO_3$

($0 \leq x \leq 1$) (GCMO) was determined for polycrystalline samples. It was realised that the GCMO samples showed CO/OO state and IMT near room temperature in the mid-doped region and magnetoresistive properties in the electron doped region, which make the samples good candidates for memristor applications [I], [III]. In the second part, after finding the optimal substrate for the materials, the magnetic phase diagram was determined for the GCMO thin films. The colossal magnetoresistance, IMT and spin memory effect were observed for GCMO thin film with x = 0.9. In the end, the role of oxygen on physical properties of the GCMO films was studied, and we showed that *in situ* vacuum and oxygen annealings can induce or remove more defects in the GCMO lattice.

2 Introduction

2.1 Manganites

Perovskite manganites are types of compounds with general chemical formula ABO_3. The A site with 12-fold oxygen coordination is occupied by a rare earth elements (La, Sm, Gd,...) or a divalent ion, the B site with manganese, Mn, is located at the centre of an oxygen octahedron with 6-fold coordination [4; 5]. The ideal cubic close-packed structure is considered for these materials (Figure 1) [6; 7; 8; 9].

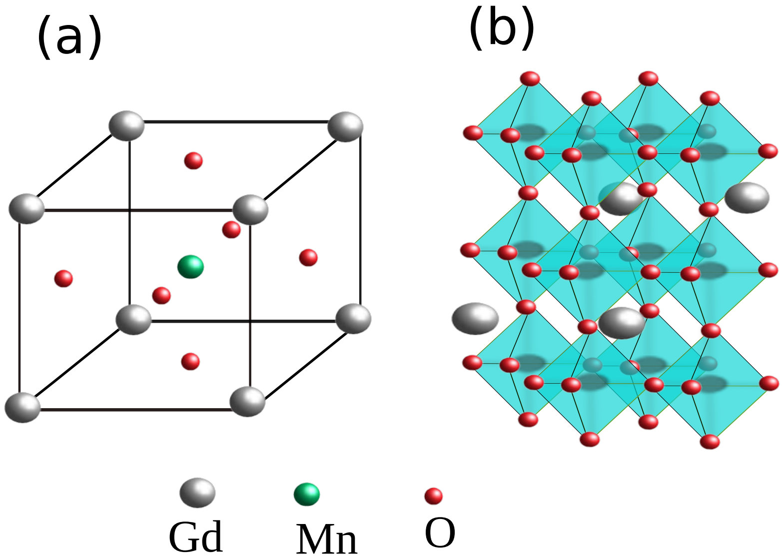

Figure 1. The ideal cubic structure (a). The crystal structure of perovskite with the oxygen octahedra (b).

The ideal cubic perovskite is distorted by several factors. Firstly, the **Ion size effects:** In the ideal cubic structure the unit cell axis, a, is geometrically related to the ionic radii in the crystal as described in the equation [10]

$$a = \sqrt{2}(r_A + r_O) = 2(r_B + r_O), \tag{1}$$

where r_i (i = A, B and O) is the ionic radii of the elements in the perovskite structure [6]. The ratio of the two expressions is called the Goldschmidt tolerance factor t, which allows us to estimate the degree of distortion. It is described as [11]

$$t = (r_A + r_O)/\sqrt{2}(r_B + r_O). \tag{2}$$

When $t = 1$, the perovskite structure has ideal cubic symmetry. If t is smaller than 1, the [BO_6] octahedra will be tilted in order to fill the space. However, the cubic structure is considered for $0.9 \leq t \leq 1$. Lower values of t lead to lower symmetry in the crystal structure, when $0.9 \leq t \leq 0.7$, the structure has orthorhombic or rhombohedral symmetry.

In mixed-valence manganites, A site is occupied with rare earth components (RE) and alkaline earth metal (AE) ($RE_xAE_{(1-x)}MnO_3$), which have different ionic radius. Therefore, the variance of A site cationic radii, σ^2, is defined as [12]

$$\sigma^2 = \langle r_A \rangle^2 - \langle r_A^2 \rangle = (x - x^2)(r_{RE} - r_{AE})^2. \tag{3}$$

By replacing trivalent rear earth metals with divalent alkaline earth metal, the oxidation state of manganese ions changes from Mn^{3+} to Mn^{4+}. Hence, by changing the doping concentration x, we can manipulate the Mn^{3+}/Mn^{4+} ratio of the manganites. The rest of this thesis will be about physical properties of this category of the materials, specifically $Gd_xCa_{(1-x)}MnO_3$.
Secondly, the **Jahn-Teller effect:** In some perovskites the distortion of the structure can be assigned to Jahn–Teller (JT) active ions at B site [13; 14; 15]. For example in $ReMnO_3$ (Re = rare earth ions) with Mn^{3+} ions the $3d^4$ electrons are divided into subshell t_{2g} and e_g to minimize the energy. Odd number of electrons in the e_g orbital causes an elongation of the MnO_6 octahedra [16].

Finally, the other key parameter to control physical properties of mixrd-valenced manganites is the effective one-electron bandwidth (or the transfer interaction of the e_g -orbital carriers),W, which depends on averaged ionic radius of the (RE, AE) cations. The smaller the radius, the smaller W, resulting in more lattice distortion [14]. However, while in the higher bandwidth manganites, the magnetic and electronic properties are mainly interpreted by the double exchange model [22], in the low bandwidth manganites, the other instabilities competing with the double exchange interaction should be considered, such as the antiferromagnetic interaction between local t_{2g} spins, the Jahn–Teller effect, and the charge/orbital ordering. Due to the small size of the Gd^{3+} ion, the GCMO family is considered a low bandwidth manganite and is usually characterized by an insulating behavior [I, III]

2.2 Magnetic interactions in manganites

The magnetic properties of manganites are mainly due to the interaction of Mn ions with each other. However, the Mn ions in the perovskite structure are too far away to have direct Heisenberg exchange interaction. Therefore, the indirect exchange mechanism [17; 18] is used to explain the magnetic long range ordering in manganites. In this thesis, the most important indirect interactions are categorized in superexchange (SE) and double exchange (DE) interactions.

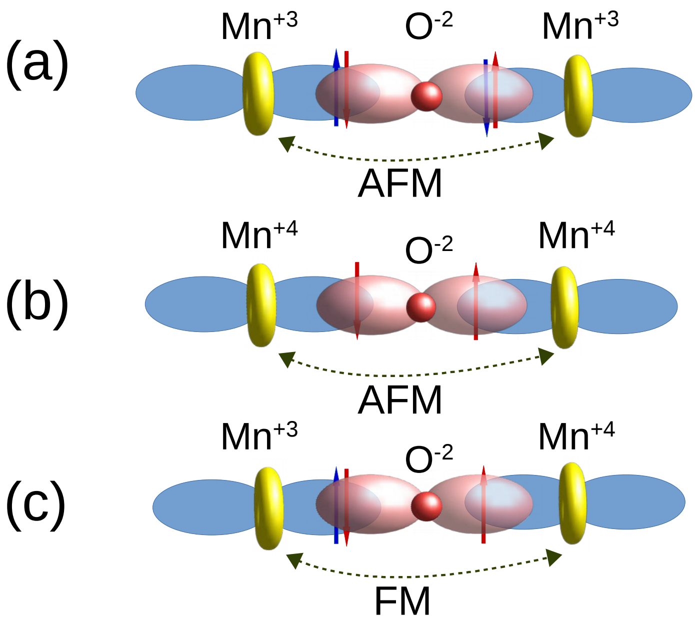

Figure 2. The Goodenough-Kanamori-Anderson rules for interaction between Mn ions in manganites (a) and (b) are superexchange interaction between Mn^{3+}- Mn^{3+} and Mn^{4+}- Mn^{4+} ions with 180 bond angle respectively, which result in AFM state. (c) shows the FM interaction between Mn^{3+}- Mn^{4+}.

SE concept can explain the interaction between two magnetic ions (Mn in manganites), which are separated by a nonmagnetic ion such as oxygen [19; 20]. The origin of the SE interaction is in the two valence electrons of the oxygen that must have opposite spins due to Pauli exclusion principle and simultaneously, each of these electrons participates in a covalent or ionic bond with one of the neighbouring Mn ions. The Goodenough-Kanamori-Anderson rules give us a striate view of superexchange interaction in different situations for $Mn^{3+/4+}$ [20; 19; 21] (see Figure 2).

According to the strong Hund's coupling, the electron spin in 3d $e_{\rm g}$ is always parallel with the local $t_{2\rm g}$ spins. However, the hybridized $2p$ orbital of oxygen and 3d $e_{\rm g}$ of Mn ion have opposite spins due to Pauli exclusion principle, resulting in antiferromagnetic (AFM) coupling. Thus, if Mn ions in Mn–O–Mn bond have the same valence, the total SE interaction is AFM, otherwise, the ferromagnetic coupling is found.

The superexchange interaction can not explain the metallic behaviour of some manganites. In this interaction, all electrons are localized resulting in insulating transport properties. To explain this discrepancy, another magnetic interaction was introduced by Zener [22], called double exchange interaction (DE). The DE interaction explains the relation between ferromagnetic state and conductive properties of manganites, especially in the hole doped region.

In mixed valence manganites, the valence states of Mn ions are a mixture of Mn^{3+} (with three t_{2g} and one e_g electrons) and Mn^{4+} (with three t_{2g} electrons). The transfer of e_g electron from Mn^{3+} to Mn^{4+} is the basic electronic mechanism in manganites. But Mn^{3+} and Mn^{4+} are too far to interact with each other directly. Hence, the indirect interaction occurs over intermediary oxygen ions. The simultaneous jumps of e_g electron of Mn^{3+} to the p-orbital of oxygen and the electron with the same spin from p-orbital of oxygen to the empty e_g of Mn^{4+} lead to the ferromagnetic (FM) state (see Figure 2(c)).

In DE interaction, the angle of Mn–O–Mn bond plays a key role as described in equation [23; 24]

$$t_{ij} = t^0 \cos(\Theta_{ij}/2), \tag{4}$$

where t_{ij} is electron's effective hopping interaction, which depends on relative angle Θ_{ij} between neighbouring i and j Mn ions. t^0 is the normal transfer integral when all the spins are aligned. The electron transfer probability and the interaction between Mn neighbours are weakened when ferromagnetic Mn–O–Mn band angle reduces from 180 degrees [25]. In manganites with strong DE interaction, the e_g electrons become delocalized in the certain Mn^{3+}/Mn^{4+} ratio at low temperature, leading to a metallic behaviour [26; 27]. While, in the materials with weak DE interaction, the coulomb repulsion among Mn^{3+} or Mn^{4+} obstructs the e_g electrons' hopping, leading to the insulating behaviour [28; 29].

2.3 Typical magnetic configurations in manganites

The physical properties of mixed valence manganites change drastically with the concentration of the divalent metal. Several structural, magnetic and charge/orbital phase transitions can be observed when the concentration increases from zero to unity. Therefore, magnetic phase diagrams of manganites were published based on theoretical treatments and experimental observations. The diagram usually interprets the magnetic state and configuration of the materials based one magnetostructure of Mn sublattice. However, in Gd based manganites, Gd magnetic moment is large enough to affect the magnetic properties in the ground state. The typical magnetic structures of Mn sublattice, which are used to describe manganites are shown in Figure 3. A, B, C and G configurations are symmetrical. A is FM along two axes and AFM along third axis, however, B is FM along the all axes. C and G, both are AFM along two axes, in third axes just C is FM. Due to DE interaction, the A and B structures can support metallic transport in the ground states of mixed-valence manganites [30; 31; 32].

One of the most interesting magnetic configuration in manganites is the CE magnetostructure, which can be interpreted as a superposition of the C and E arrangements. The structure has been written as $C_{1-x}E_x$, where x is hole concentration. The $C_{0.5}E_{0.5}$ magnetostructure is the ideal case, as schematically shown in Figure 4. In the association with CE–type structure, the small or medium bandwidth half doped manganites show charge and orbital ordering state (CO/OO) [12; 33]. The CO/OO state is coupled with JT distortion. In the effect of JT coupling, the $3x^2 - r^2$ or $3y^2 - r^2$ orbitals at the Mn ions are ordered ferromagnetically in planes and an-

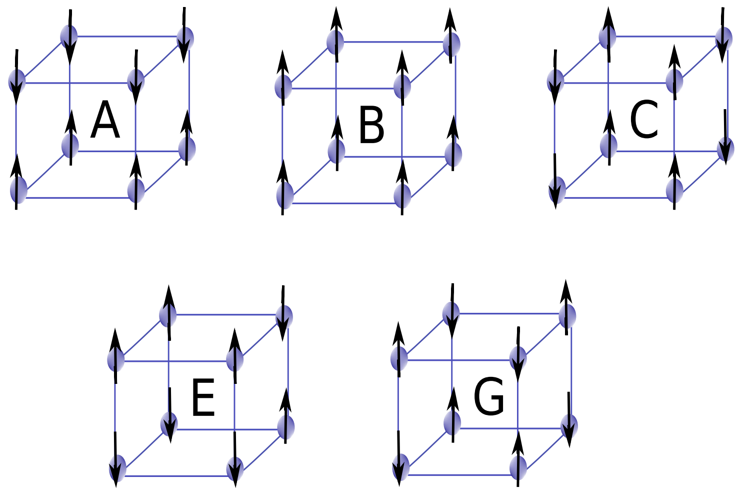

Figure 3. The most common magnetic structures, which are used to describe magnetic properties of manganites.

tiferromagnetically between planes (see Figure 4). In the CE-type ordering, Mn^{3+} and Mn^{4+} ions are arranged as in a checker board and the Mn^{3+} sites are JT distorted. Furthermore, the distortion traps the electrons and makes the materials insulating [34; 35; 36]. Upon the CO/OO transition, the insulating CE-type AFM state is formed. However, the CO/OO-ordered insulator can change to metal ferromagnetic state under a large external magnetic field [37; 38]. The CO transition is of the first order, which is sometimes accompanied by a structural transition due to strong electron–lattice coupling [39; 40; 41].

2.4 Cluster spin glass model and phase separation

Cluster glass (CG) is kind of spin glass, in which a group of spins are locally ordered, creating small domains that interact with other spins. CG behaviour is the result of A-site disorder in manganites. The substitution of the trivalent A-site with different divalent ions (like alkaline elements) changes the average A-site ionic radius of the parent manganites, affecting directly the bandwidth of the material [42; 12; 43; 44]. This type of substitution also promotes A-site disorder due to random distribution of the A-site cations with different variance (σ, see section 1). The disordering can induce phase separation in the components. The FM metal-insulator transition as well as AFM interactions in the doped-manganites cause the systems to divide in two different phases below the Curie temperature. One of them is the low resistive metallic phase, which magnetically has FM character with domination of double exchange interaction. The other one is a high resistive insulating phase, probably

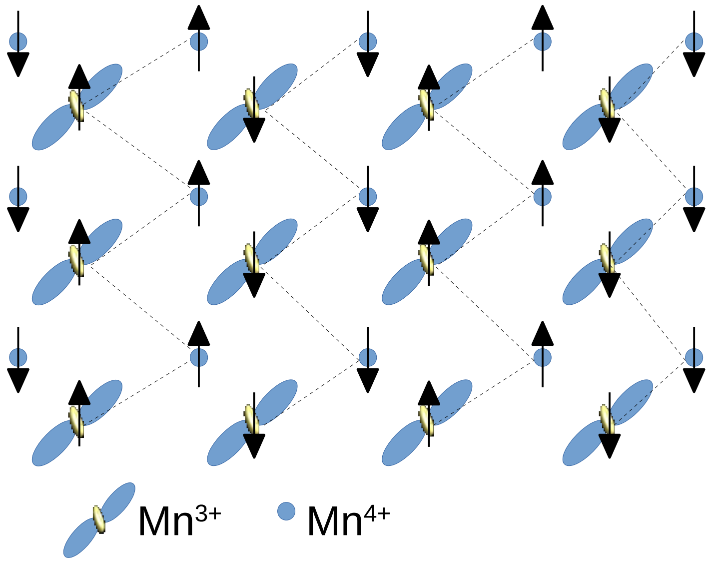

Figure 4. The charge and orbital ordering states of Mn ions in Mn–O plane, which are the result of CE type magnetostructure.

having AFM character or even a canted spin state.

2.5 The colossal magnetoresistance properties

The correlation between resistance and magnetic field can be understood from magnetoresistance (MR) phenomena, i.e. the magnetoresistance is defined as a change in resistance by application of an external magnetic field. Mathematically magnetoresistance can be defined as

$$MR = \frac{(R_{\mathrm{H}} - R_0)}{R_0}, \tag{5}$$

where R_{H} is the resistivity in an applied magnetic field and R_0 is the resistance in zero magnetic field. When the magnitude of change in resistivity is very large, the effect has been termed as colossal magnetoresistance effect (CMR). The negative CMR effect has been observed in many mixed-valence manganites [5; 45; 46]. These materials have paramagnetic insulating phase at high temperature and, upon cooling, resistivity increases sharply. With further cooling, the metallic-ferromagnetic transition has been observed at low temperature. With application of external magnetic field of a few teslas, the resistivity peak is suppressed, generating the CMR effect. The transport mechanism and ferromagnetic metallic phase were discussed earlier through the DE mechanism [22]. However, Millis et al. [28] pointed out that the DE interaction alone can not explain the details of the CMR behaviour. In particular, the DE model fails to explain the high electrical resistivity of the paramagnetic phase. They suggested that the high resistivity can be attributed to a strong electron-lattice interaction via lattice-polaron formation. A lattice-polaron is a charge carrier, trapped in the elastic deformation, which it has created. In manganites, the polarons are directly related to the JT distortion. The JT interaction tends to lift the degeneracy of the $3d$ orbital and deforms MnO octahedra. However, the JT interaction diminishes with increasing doping level. Then the insulating/metallic phase separation is another field-dependent factor critical for the observed CMR effects. These can be interpreted on the basis of electronic delocalization and localization phenomena, which induce a competition between ferromagnetism and antiferromagnetism in such systems.

2.6 The role of oxygen

Large amount of conducted research has pointed out that the properties of the complex perovskite manganites are mainly due to the ratio of different oxidation states of manganese ions [47; 48], [I]. One way to tune the ratio of Mn^{3+}/Mn^{4+} is the substitution of divalent alkaline elements in A-site in the perovskite structure [49; 7; 8]. However, most transition metal perovskites exhibit oxygen non-stoichiometry, the correct chemical formula is $ABO_{3-\delta}$ instead of the nominal formula, e.g. ABO_3, where A is rare earth ions, B is transition metal and δ describes the degree of oxygen vacancies. In these materials, changing valence of the transition metal can balance the change due to the formation of oxygen vacancies. Since the amount of oxygen vacancies is directly linked to the average oxidation state of the transition metal, change the oxygen stoichiometry is another way to change the Mn^{3+}/Mn^{4+} ratio in manganite thin films [50; 51].

Oxygen non-stoichiometry of materials is generally manipulated by annealing in different atmospheres, which results in significant change in magnetic and transport properties [13; 52]. The annealing temperature is significantly lower than the synthesis temperature since oxygen becomes mobile at lower temperatures than cations. Annealing materials in a reducing atmosphere, meaning a low oxygen partial pressure $p(O_2)$, will increase the number of oxygen vacancies and the δ in $AMnO_{3-\delta}$ [84]. In contraste, annealing materials with oxygen vacancies in an oxidizing atmosphere with a high $p(O_2)$), will add oxygen to the materials lattice by filling those vacancies [VI]. In manganites, when δ=0, there is no oxygen vacancies, the oxygen annealing can lead to the formation of cation vacancies on the A and B sites, resulting in formation of $AMnO_{3+\delta}$ compositions as opposed to $AMnO_{3-\delta}$ or plain $AMnO_3$.

2.7 The magnetocaloric effect

The magnetocaloric effect (MCE) is a magneto-thermodynamic phenomenon, in which the thermal state of magnetic materials changes in response to changes of the applied magnetic field [53; 54]. In isolated conditions, when the external magnetic field is applied on magnetic materials with random orientation of magnetic spins, the spins align themselves with the external field direction, resulting in decreasing magnetic entropy. However, to keep the total entropy constant, the lattice and electronic entropies increase, leading to increased temperature of the materials. After removing the heat energy, the magnetic field is decreased adiabatically, ending up with the increased magnetic entropy. This leads to the cooling of the materials. In this stage, if the magnetocaloric materials are in thermal contact with a heat environment, heat energy transmits into the materials. When the materials and the environment are in in thermal equilibrium, the cycle can restart [55; 56; 57].

To have a desired magnetic refrigerator, such magnetocaloric materials need to undergo magnetic transition with a large entropy change, ΔS and refrigerator capacity, RC. These quantities are defined by [53; 54]

$$\Delta S(T) = \mu_0 \int_0^{H_{\max}} \left(\frac{\partial M}{\partial T} \right)_H \mathrm{d}H, \tag{6}$$

$$RC = \int_{T_{\min}}^{T_{\max}} |\Delta S(T)| \, \mathrm{d}T. \tag{7}$$

Here T is the temperature (K), H the magnetizing field (Am^{-1}), M the magnetization (Am^{-1}) and μ_0 the permeability of vacuum (TmA^{-1}). $H_{\max}$ is the highest applied magnetizing field, and $T_{\min}, T_{\max}$ are usually taken to delimit the full width at half maximum (FWHM) of the peak in $\Delta S(T)$ associated with the magnetic transition.

2.8 $Gd_{(1-x)}Ca_xMnO_3$

(Gd, Ca)MnO_3 is considered a low bandwidth manganite with small A-site ionic radii, smaller than Sm and Pr, and with a high net magnetization. There are few comprehensive studies about the family, probably due to the large neutron absorption cross section of Gd. This in turn caused the failure of the study of magnetic phase diagram of (Gd, Ca)MnO_3. Prior to this work, there were no detailed data on the crystal and magnetic structures of the Gd manganite systems which, on the other hand, play an important role in explaining all the physical properties of these compounds. In this thesis, we investigate the structural, magnetic and electrical properties of $Gd_{(1-x)}Ca_xMnO_3$ ($0 \leq x \leq 1$) components as a bulk and thin films to provide phase diagram of the perovskite manganites.

3 Experimental details

3.1 Sample preparation

3.1.1 Solid state reaction method

The conventional solid state reaction method was used to synthesize polycrystalline GCMO compounds at Ca doping intervals of Δx = 0.1. The following synthesis recipe was designed to have GCMO bulk material without impurity phases such as Mn_3O_4, a typical magnetic impurity phase in manganites [58; 59]. The synthesis route was previously developed for PCMO [60]. For GCMO, gadolinium(III) oxide (Acros Organics, 99.9+%), calcium carbonate (Merck Millipore, 99+%) and manganese(IV) oxide (Alfa Aesar, 99.9+%) were used as raw materials. The Gd oxide was calcinated at 1600 °C and the calcium carbonate was dried at 200 °C overnight to remove hydroxide and carbonate phases before the powders were weighed according to stoichiometric formula to obtain 5 g of each sample. The dried powders mortared by hand and compacted into pellets (5 min at 30 MPa). The pellets were initially calcinated at 750 °C for 60 h. Then they were mortared, recompacted again and sintered at 1300 °C for 24 h in air until the equilibrium structure was obtained. The crystalline structure and the chemical phase purity of the samples were investigated by x-ray diffractometry (XRD) together with Rietveld analysis using the Maud program [61].

3.1.2 Pulsed laser deposition

Pulsed laser deposition (PLD) is a physical vapour deposition method that uses high energetic laser light to energize material, creating a deposition vapour that can be condensed on any possible substrate [62]. A schematic illustration of the PLD setup is presented in Figure 5. In the film deposition process, the pulses of high energy laser beam are focused on a target material. The material is then vaporized and the cloud of particles, called ”plume” is produced. The plume condenses as a film on a substrate facing the target in a proper deposition conditions. The process can occur in ultra high vacuum, in the presence of a background gas such as oxygen, which is usually used when preparing the thin films of complex oxides. The advantages of the PLD technique are that the technique can be used for a wide range of materials to have stoichiometric thin films, just by optimization of the deposition conditions such as the choice of an appropriate substrate material, deposition temperature, laser fluence, number of pulses, pulse frequency and deposition pressure. Like many other manganite thin films [63; 64; 65; 48], the GCMO ($0 \leq x \leq 1$) thin films were prepared by PLD method in a deposition conditions, which had been optimized previously [66].

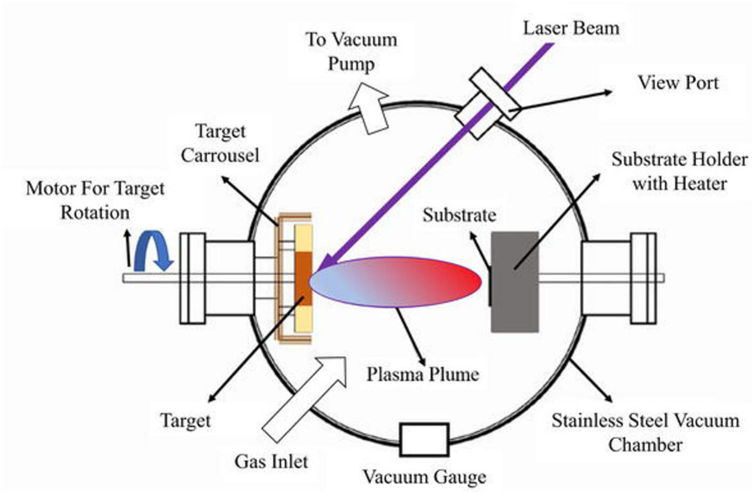

Figure 5. Schematic illustration of the pulsed laser deposition setup.

In this work, all epitaxial GCMO thin films with varying Ca concentrations were fabricated by pulsed laser deposition (PLD) method on oriented $(00l)$ substrates. The pure polycrystalline GCMO pellets, which were synthesized via the solid state method [I], were used as deposition targets. Before the deposition, the chosen substrate is heated up to 700 °C with a rate of 25 °C/min and under the oxygen background gas with a total pressure of 174 mTorr. The list of substrates used in this work is presented in Table 2 of section 4. Since the lattice parameters of the GCMO bulk samples and the substrates are different, it is expected that the films grow in the diagonal direction of the substrate unit cell to minimize the lattice mismatch between substrate and the films. The illustration in Figure 6 shows the growth direction of GCMO films on STO substrate.

The ablation process was carried out by XeCl-laser with a wavelength of 308 nm and an energy density of 2 J/cm^2. To keep the deposition condition the same for all the films, 1500 pulses with a rate of 5 Hz were used for preparation of the all films. Then, the films were post-annealed in an atmospheric pressure of oxygen for 10 min at deposition temperature, after which the temperature is decreased back to room temperature with a cooling rate of 25 °C/min. The growth rates of the GCMO films with various doping concentrations deposited on STO substrate are shown in Figure 7. As can be seen, the rate increases with increasing Ca concentration. This can be related to the densities of the compound and the sintered target. As heavier rare earth ions of Gd are substituted by lighter ions such as Ca, the density of the compound and thus also the target reduces. This can lead to thicker films when the same number of pulses was applied to the target.

In order to investigate the effect of oxygen content on magnetic and transport properties of the GCMO thin films, the *in situ* annealing was done for two chosen Ca concentrations. In oxygen treatment process, the deposition condition is similar to the above mentioned process, except that at the final stage the films were kept in atmospheric pressure of oxygen for 60 min. In vacuum treatment process, after the

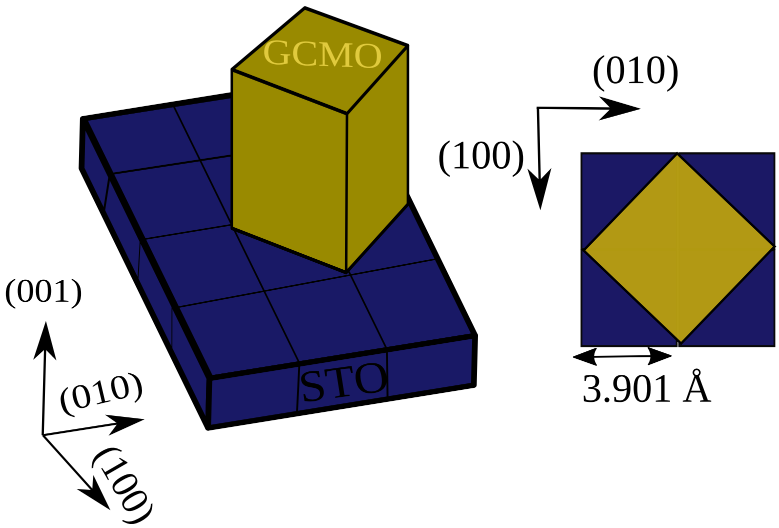

Figure 6. A schematic illustration of GCMO thin film grown on STO substrate, which shows the 45° rotation between the GCMO and STO lattices.

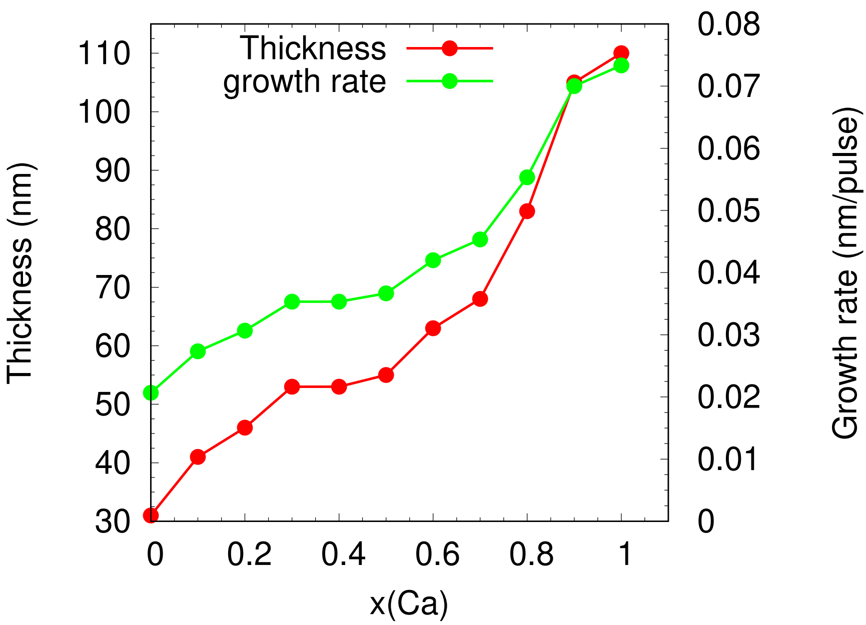

Figure 7. Thicknesses and growth rates of the GCMO films with different Ca concentrations deposited with 1500 pulses.

Table 1. Details of the x-ray diffraction setup parameters used to obtain XRD patterns for polycrystalline bulk and thin film GCMO samples by Philips X'Pert Pro diffractometer and Empyrean diffractometer.

Setup details	Philips X'Pert Pro diffractometer	Empyrean diffractometer
X-ray tube	Empyrean Cu LFF	Empyrean Cu LFF HR
	40 kV 45 mA	40 kV 45 mA
Soller slit	0.04 rad $\times 2$	0.04 rad $\times 2$
Filter	Nickel	Bragg HD monochromator
Divergence Slits	1/4 $^\circ$	1° and 1/2 $^\circ$
Antiscatter Slit	7.5 mm	7.5 mm
Mask	10 mm	4 mm
Goniometer	Schulz	Five axis
Detector	PIXcel1D	PIXcel3D

deposition, the films were treated at the pressure of 4×10^{-4} Torr for 10 min.

3.2 Structural characterization

3.2.1 X-Ray diffraction

X-ray radiation has a wavelength in the range of the typical distances between atoms. Thus, it can be used to probe crystal structures. Nowadays, crystal structure and phase identification are studied largely by x-ray diffraction technique (XRD). The technique is based on constructive interference of monochromatic x-rays when diffracted from elements in lattice sites of a periodic crystalline structure. The relation between crystal structure and measurement setup are described geometrically by Bragg's law [67]

$$n\lambda = 2d\sin(\theta), \tag{8}$$

where d is distance between lattice planes, λ and θ are wavelength and angle of incoming radiation to the lattice, respectively, and n is an any positive integer. Thus, every crystalline structure has its own reflection patterns due to diffractions. In powder samples, due to random orientation of crystallites, all diffractive reflections can be detected by measuring the reflected radiation intensity vs. the reflection angle, $I(\theta)$, over a circular arc, which contains the radiation source centred around the sample. The room temperature structural properties of the GCMO powders were investigated by 2θ XRD scans within the range of 20° – 110° using Philips X'Pert Pro diffractometer with Schulz goniometer at room temperature. The details of this setup are given in Table 1. The results were analysed with the Maud-Rietveld refinement program [61].

In the case of thin films, to obtain XRD pattern in different directions, the measurement setup should be aligned in specific diffraction angle according to the substrate. The XRD measurements for GCMO thin films were done by using Philips Empyrean diffractometer with a five axis goniometer (see Table 1 for more details). To confirm the phase purity and to calculate c-parameter of the GCMO films, θ-2θ scan in the range of 20° – 110° was implemented in $(00l)$ direction. In addition, the quality of the films, was confirmed by θ-2θ scan in $(0hl)$ and (khl) directions and by ϕ-θ scan of the (224) peak.

3.2.2 X-ray reflectivity

X-ray reflectivity (XRR) is a surface sensitive technique, which is based on reflected x-ray beam from the sample surface. Such a measurement can provide information on thickness, roughness and interfacial properties of thin films. When the incident beam comes into a material, the beam is partially reflected from the surface and partially refracted into the material.

At the certain angle, so-called critical angle (θ_c), the incoming beam is reflected completely. The θ_c for the case of x-ray scattering, can be written as [68]

$$\theta_c = \arcsin(1/n), \qquad \theta_c = \lambda\sqrt{\rho/\pi}, \tag{9}$$

where λ is the wavelength of the incident beam and ρ is the electron density for x-rays. From this equation, the higher ρ results in larger θ_c, which means the higher density of materials.

For angles of incidence above critical angle, when the beam transmitted into the sample, it reflected partially. The intensity of the reflected beam drops approximately with a factor Q^{-4} for an ideal flat surface, which is referred to as Fresnel reflectivity [69; 70]. Figure 8 illustrates different conditions when the incident angle of the x-ray is smaller, equal to, and greater than the critical angle for total reflection. However, the decay of the reflectivity from a thin layer is qualitatively different and it shows oscillations with a period of ΔQ=2π/d, where d is the film thickness. The oscillations are called as Kiessig fringes [71]. By measuring the separation of the maxima of the fringes, the film thickness can be determined. The rough surface or interface can diffuse the incident beam, leading to decreasing intensity of the oscillations with increasing incident angle. Thus, the decay rate of the oscillations can be proportional to the surface roughness. In the layered systems, the rough interface can drastically decrease the reflected intensity with increasing incident angle. As a result, the amplitudes of the fringes are damped (see Figure 9).

3.2.3 Transmission electron microscopy

Transmission electron microscopy (TEM) is a technique in material science to recognise crystal structure and crystal defects like dislocation, grain boundary and misorientation. The basic working principle in TEM is similar to the that of light microscope but electron is used instead of light. The electrons' beam emitted from the electron gun go through a condenser lens to be coherent and focused before it transmits the sample. The transmitted beam is focused by the objective lens into an image on fluorescent screen. Then the images are magnified by an projector lenses. Due to the shorter wavelength of electrons in comparison to that of light, the resolution of TEM images is much higher.

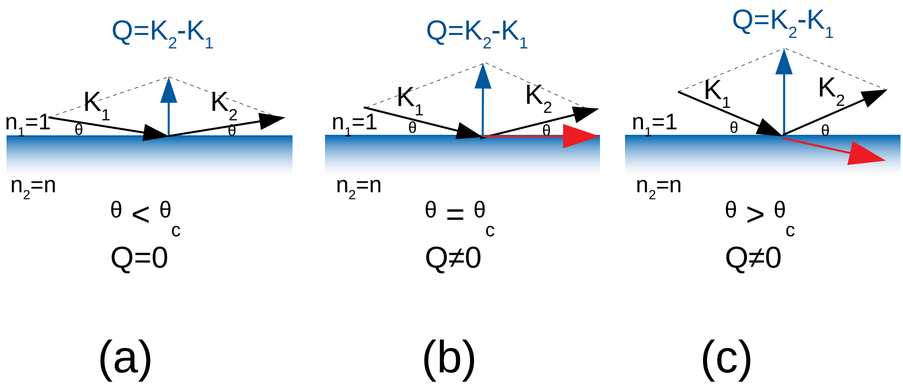

Figure 8. Reflection and refraction of x-rays at material surface with the changes in the grazing angle. (a) The incident angle is smaller than critical angle; all incident x-rays are reflected. (b) The angle is equal to critical angle; the incident x-rays are propagated partially along the sample surface. (c) The incident angle is larger than critical angle; some part of incident x-rays penetrate into the sample. The red arrow shows refracted beam.

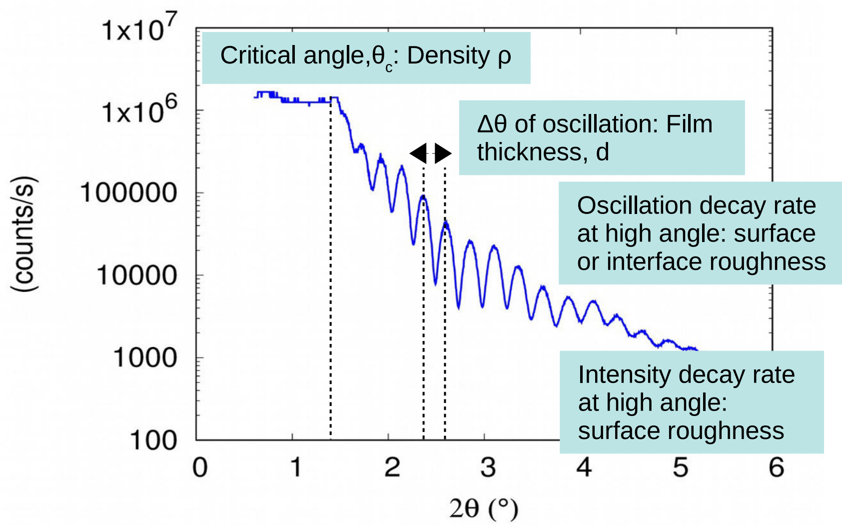

Figure 9. Information provided by x-ray reflectivity profile.

In this research, the cross sectional TEM measurements were done to explore crystallographic structure by using the JEOL JEM-2200FS electron microscope combined with a 200 kV field emission gun (FEG) and in-column energy filter (Omega Filter). In addition, in order to determine the films' thickness, a probe-corrected scanning TEM with high-angle annular dark field imaging (HAADF STEM) were performed with TITAN 80–300 at the voltage of 200 kV. All the TEM measurements were done by the facility staff of Aalto University, Finland.

3.3 X-ray photoelectron spectroscopy

In x-ray photoelectron spectroscopy (XPS) set up, when an inelastic collision occurs between the high energy x-ray photons and the electrons in a specific bound states of sample, the electrons can receive energy from the photons to be excited. The sufficient amount of energy leads to emission of excited electrons from the materials surface. Electrons are ejected from the sample surface when the sample is bombarded with x-ray photons. Once these electrons are in the vacuum, they are collected by an electron analyser, which measures their kinetic energy. The electron energy analyser produces an spectrum of intensity of the emitted electrons versus their binding energy [72]. In manganites, knowing the Mn^{3+}/Mn^{4+} ratio is the crucial knowledge for understanding the magnetic and electrical properties. For this aim, XPS technique is widely used to learn about electronic state of the materials' elements [73]

In this research, the x-ray photoelectron spectroscopy measurements were done using Thermo Scientific Nexsa system with pass energy of 50 eV to scan the core-level spectra. The spectra were collected by monochromated Al Kα radiation and dual beam charge compensation. All the measurements were preformed by the Material Science Laboratory at University of Turku, Finland.

3.4 Positron annihilation spectroscopy

Positron annihilation spectroscopy (PAS) measurements are conducted to identify vacancy type defects and their concentrations in materials. In this technique, the accelerated and monoenergetic positrons are implemented into a sample in the range of energy (E_p) between 0.05–35 keV. Once the positrons interact with the electrons in the sample, they lose their kinetic energy due to annihilation with electrons in delocalized lattice sites or in localized vacancy like defects, which leads to emission of gamma photons. The broadening of the gamma photons, which is characterised as a S parameter, is a fraction of positron annihilating with low momentum valence electrons and represents vacancy type defects and their concentration.

Positron annihilation lifetime spectroscopy (PALS) measures the elapsed time between the implantation of the positron into the material and the emission of annihilation radiation. The spectra can be deconvoluted into three lifetime components, which are direct evidence of delocalized annihilation (bulk annihilation, τ_B) and localized annihilation at two different defect types (τ_1 and τ_2). The corresponding intensities reflect the concentrations of each defect type.

In this work, the effect of *in situ* vacuum and oxygen annealing on vacancy like defects and their relative concentrations were investigated in GCMO with x=0.4 and 0.9 by positron annihilation spectroscopy technique. The experimental measurements were carried out at ELBE at the Helmholtz-Zentrum, Dresden-Rossendorf, Germany.

3.5 Magnetometry

The magnetic properties of the GCMO samples were measured by superconducting quantum interference device magnetometer (SQUID). The SQUID device used in this research was commercially available Quantum Design MPMS radio frequency SQUID magnetometer. The device consists of a superconductor loop including Josephson junction and a pick-up coil. Once a sample moves through the pick-up coil, the magnetic flux is altered, consequently inducing a current in the coil according to the Lenz law. The current is detected and converted to the radio frequency signal by LC tank-circuit, which is kept in the liquid helium bath. The electrical system of SQUID amplifies the signal, which can be used for creating the magnetic moment of the sample.

For GCMO samples, the measurements were done in zero field cooled (ZFC) and field cooled (FC) modes to understand the magnetization behaviour as a function of temperature between 10–400 K in a constant magnetic field. Magnetic hysteresis loops were recorded between $\pm$5 T fields at various temperatures.

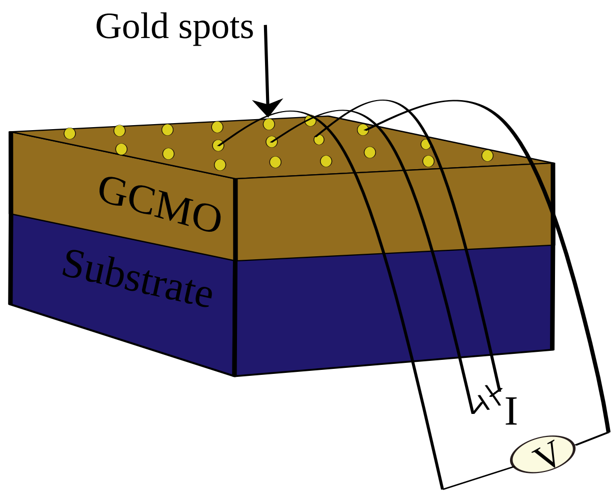

Figure 10. The illustration shows the GCMO film, where the Au pads were sputtered to make appropriate contacts for resistivity measurements.

3.6 Magneto-transport measurements

Temperature and field dependence of resistance properties of the GCMO bulk and thin films were measured by Quantum Design Physical Property Measurement System (PPMS). By applying a current of 50 μA, the zero field cooled (ZFC) and the field cooled (FC) with an external magnetic field of 9 T scans were carried out for measuring resistivity as a function of temperature $R(T)$ between 10–350 K to find the metal-insulator transition. The magnetoresistance properties $R(H)$ were measured at low temperature and room temperature (RT) by applying $\pm$9 T magnetic field. To implement the measurements by PPMS, the Au pads were sputtered on the surface of the GCMO films to have a good contact for wire bonding, as shown in Figure 10.

4 Results and discussion

4.1 Polycrystalline GCMO

4.1.1 Structural properties

The phase purity and crystal structure of the polycrystalline GCMO samples were explored by XRD measurements at room temperature. The XRD data were analysed by Rietveld refinement method. The goodness-of-fit , χ^2, of the phase calculation was below 2 for all samples, indicating a satisfactory agreement between the data and the model. The experimental XRD data and Rietveld fit of all samples obtained from [I] are shown in Figure 11. The data revealed that all samples are well crystallized with orthorhombic space group Pnma. However, the orthorhombicity factor ($\frac{b}{a}$) decreases while Ca concentration increases, having the upper limit for the Ca doping, $x = 1$, $a \approx b \approx \frac{c}{\sqrt{2}}$, which means that tetragonal symmetry is dominant. The lattice parameters of all samples are listed in Table 2 and also presented in [I].

As the average ionic radii calculated from Eq. (2) increases with increasing Ca doping level, the tolerance factor increases, reaching the ideal value of 1.0 according Eq. (1) (see Table 2). This means that the lattice distortion decreases while Ca concentration increases. This can be explained by replacing smaller ion, Gd, with larger ion, Ca, which could increase the average ionic radii and decrease deformity of the unit cell. On the other hand, by doping Ca^{2+} in Gd^{3+} sites in the GCMO components, the Mn oxidation state changes from Mn^{3+} to Mn^{4+}. As the Mn^{3+} concentration decreases, the JT distortion is weakened in the crystal lattice. However, the average cation radius values in A-site $\langle r_A \rangle$ for GCMO are smaller than those of SCMO and PCMO. Thus, GCMO is highly distorted in comparison with polycrystalline SCMO and PCMO [75].

4.1.2 Phase diagram of polycrystalline GCMO

Mixed valence perovskite manganites $RE_{1-x}A_xMnO_3$ (RE = rare-earth cation, A = alkali or alkaline earth cation) show varied physical properties, as the concentration x of divalent A cations changes from zero to unity. The substitution not only changes the valence of the Mn but also affects the average A-site cationic radius ($\langle r_A \rangle$), $\langle r_A \rangle$ = $(1-x)r_{RE} - xr_A$, and A-site cationic size mismatch, which is quantified by the variance of $\sigma^2 = \langle r_A \rangle^2 - \langle r_A^2 \rangle = (x - x^2)(r_{RE} - r_A)^2$ [32; 41; 76]. Thus, the system goes through different phase transitions, which stand for various structural, magnetic, charge and orbital ordering transitions [5; 4]. In low bandwidth manganites, the electrical and magnetic phase diagrams of Sm-based and Pr-based manganites have been widely investigated by neutron diffraction measurements [9; 77]. The

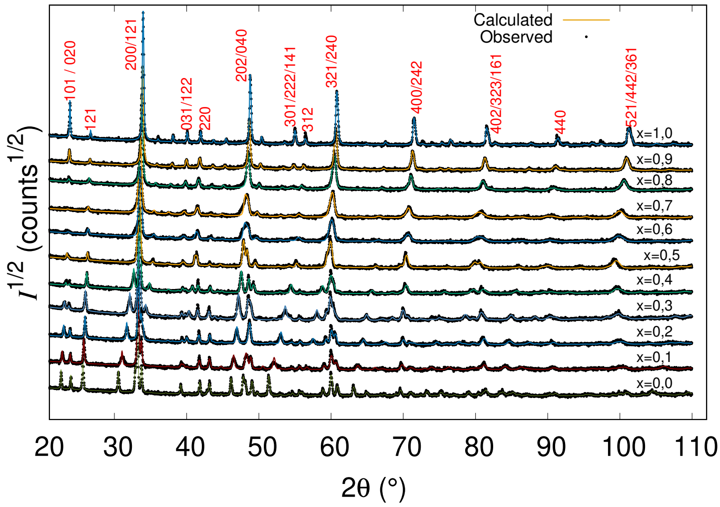

Figure 11. The room temperature XRD measurements of the GCMO samples with Ca concentration between 0.0-1. All the patterns were fitted by Rietveld analysis and the diffraction peaks are labelled according to the space group Pnma [I].

Table 2. Lattice parameters, an average size and disordering of the cation A, tolerance factor (t) and a cell volume of GCMO obtained from the XRD data at room temperature. The cation radii are taken from Shannon tables for ninefold coordination [74].

x	a (Å)	b (Å)	c (Å)	$\langle r_A \rangle$ (Å)	σ^2 (10^{-4}Å^2)	t	V_{cell} (Å^3)
0.0	5.317(4)	5.861(3)	7.436(3)	1.078	0	0.84(1)	230.71(3)
0.1	5.311(1)	5.765(1)	7.459(5)	1.084	3.45	0.85(3)	227.92(3)
0.2	5.314(2)	5.642(2)	7.489(3)	1.090	6.15	0.85	223.93(4)
0.3	5.335(1)	5.569(1)	7.504(8)	1.096	8.07	0.86(4)	222.98(4)
0.4	5.347(2)	5.501(3)	7.518(7)	1.102	9.22	0.86	218.88(4)
0.5	5.348(4)	5.396(4)	7.523(6)	1.109	9.61	0.87(5)	217.14(3)
0.6	5.333(1)	5.375(3)	7,505(5)	1.115	9.22	0.87(1)	215.15(5)
0.7	5.313(2)	5.317(2)	7.552(1)	1.121	8.07	0.87	214.64(4)
0.8	5.296(5)	5.336(1)	7.489(2)	1.127	6.15	0.88(2)	211.67(3)
0.9	5.282(6)	5.307(3)	7.472(2)	1.133	3.45	0.88	209.49(2)
1.0	5.269(1)	5.284(4)	7.457(4)	1.140	0	0.89(2)	208.0(4)

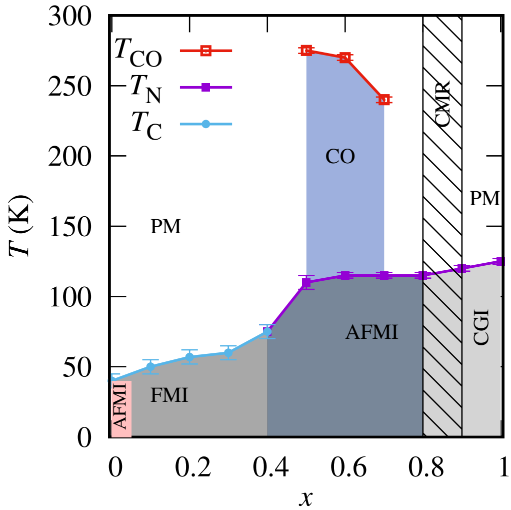

Figure 12. The magnetic phase diagram of GCMO. T_C, T_N and T_{CO} are deduced from $M(T,H)$ and $R(T,H)$ measurements. PM stands for paramagnetic state, FMI for ferromagnetic insulator, AFMI for antiferromagnetic insulator, CGI for cluster glass, CO for charge ordering. The dashed area indicates the region, where the magnetoresistivity properties (CMR) exist [I].

$Sm_{1-x}Ca_xMnO_3$ (SCMO) components, with low $\langle r_A \rangle$ (1.132 – 1.18 Å) and small σ^2 (5.8×10^{-4} Å^2), exhibit CMR only on the electron doped side ($x > 0.55$) [9; 78]. The $Pr_{1-x}Ca_xMnO_3$ series (PCMO), with zero size mismatch i.e. a constant $\langle r_A \rangle$ value (1.18 Å) due to identical size of Ca and Pr [77], show CMR on both hole doped and electron doped regions [9; 77].

However, the magnetic phase diagram of the Gd-based manganites has not been investigated due to the large neutron absorption cross section of Gd ions. Gd has small ionic radii, smaller than Sm and Pr, but higher net magnetization. In this research, we investigated the GCMO magnetic phase diagram. The XRD data, the temperature and field dependence of the magnetization, resistivity and magnetoresistive properties of the compounds within the complete Ca doping range were utilized [I] and the results were compared with SCMO and PCMO.

Figure 12 shows the magnetic phase diagram of GCMO through the whole Ca concentration, x [I]. The magnetic structures found in GCMO are diverse, but three main regions can be recognized in the phase diagram.

Low Ca-doped region ($0.0 \leq x \leq 0.4$)**:** In this region, all the samples show a maximum below Curie temperature, T_C, in $M(T)$ curves as shown in Figure 13(a). It means that the magnetization increases as temperature decreases. Upon further cooling, the magnetization declines and goes to the negative values. This behaviour can be attributed to two magnetic sublattices, Mn and Gd. The stronger $3d$ exchange interaction when compared to that of $4f$ makes the Mn–Mn coupling stronger than Gd–Mn. Therefore, the ferromagnetic ordering of Mn ions dominates below T_C, resulting in increased magnetization. As the temperature decreases, the antiferromagnetic ordering of Gd-Mn coupling grows rapidly and the magnetization decreases. When $M_{Gd} > M_{Mn}$, the magnetization goes to the negative values. Around 20 K,

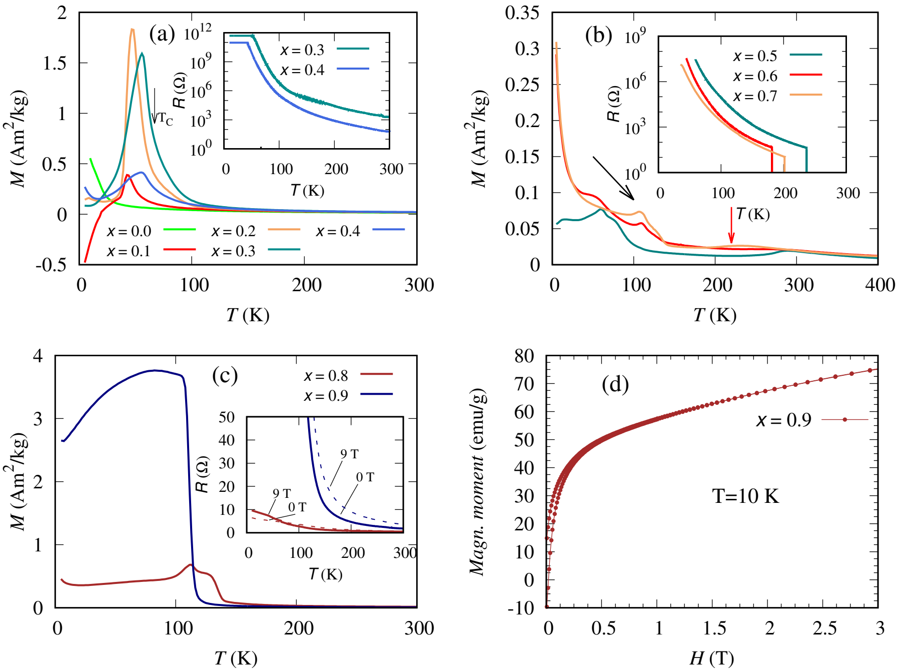

Figure 13. Temperature dependence of the magnetization M measured in 10 mT field for the samples (a) in the low Ca-doped region ($x \leq 0.4$), (b) in the middle range Ca-doped $0.5 \leq x \leq 0.7$ and (c) in the high Ca-doped region ($0.8 \leq x \leq 1$). The determined T_C for $x = 0.3$ is shown by the arrow. The AFM and charge ordering transitions for sample with x=0.7 are shown by black and red arrow at roughly 100 K and 200 K, respectively. The insets show the resistivity R measured at temperatures between 10 and 300 K. The resistance drops to below 1 Ω for all samples in the middle range Ca-doped region at high temperature. In (a) and (b) the resistance data below 50 K is artificially saturated due to hardware limitations. (d) The part of the hysteresis loop for GCMO sample with x = 0.9 measured at 10 K [I].

the magnetization rises up again and becomes positive. This can be explained so that the external magnetic field overcomes the local field produced by Mn sublattice and magnetic moments of Gd ions orient along the external field direction. With knowledge of this, we can say that the GCMO samples are ferrimagnetic at background state. Moreover, due to large lattice distortion, which weakens DE interaction, all the samples show insulating behaviour in the range of temperature 10–300 K (see the inset of Figure 13(a)). At the end, it is clear in this Ca doping region that the GCMO samples change from paramagnetic insulator to ferromagnetic insulator at T_C.

Mid Ca-doped region ($0.5 \leq x \leq 0.7$)**:** The temperature dependence of magnetization measurements shows a hump near room temperature for all samples in this region (Figure 13(b)). This hump can be attributed to the CO/OO state, which also has been observed in other low bandwidth manganites such as SCMO and PCMO [9; 77]. The highest T_{CO}, where the charge ordering is maximum, was observed for sample with $x = 0.5$. However, the highest T_{CO} value was obtained for $x = 0.6$

in SCMO and PCMO series [30; 32]. Similar to SCMO, the $M(T)$ curves exhibit a transition around 100 K. The transition can be referred to AFM ordering of Mn ions in these concentrations. In this Ca doping region, the resistance below the magnetic ordering temperature, (T_{N}), is large but drops to the low level at high temperature. The transition temperature deduced from $R(T)$ curves coincides with appearance of charge ordering phase temperature deduced from $M(T)$ curves. The high conductivity at T_{CO} could be due to the dielectric breakdown of the charge ordered state, accompanied by the great number of charge carriers, leading to the metallic state [38]. According to the $M(T)$ and $R(T)$ results and comparison with other low bandwidth manganites [38; 79; 80], we can say that the GCMO samples with $0.5 \leq x \leq 0.7$ are AFM insulators (AFMI) below T_{N} and present charge ordering phenomena above T_{N}. As reported earlier, the magnetic structure of the manganites, which show the combination of AFMI state and CO state with $T_{\mathrm{N}} \leq T_{\mathrm{CO}}$, are of CE or C-type structure.

High Ca-doped region ($0.8 \leq x \leq 1$): The components in this doping range correspond to Mn^{4+} rich region or electron doped region, where the behaviour of magnetic cluster can be observed. It is assumed that there is ferromagnetic double exchange interaction between Mn^{3+}–Mn^{4+} ions in the nonferromagnetic matrix. This matrix is due to the antiferromagnetic superexchange interaction between Mn^{3+}–Mn^{3+} and Mn^{4+}–Mn^{4+} pairs. At lower border of this region, the AFM ordering is dominated and AFM transition in $M(T)$ curves is observed around 100 K. Instead, the $R(T)$ curves exhibit a transition in this temperature from a semiconducting to an insulating state with sharp increase in resistivity.

With increasing Ca concentration, $x = 0.9$, the volume of FM phase increases and thus the magnetic cluster glass behaviour can be observed in FC and ZFC curves (Figure 13(c)). The FC curve exhibits ferromagnetic like behaviour, which means that the magnetization rises significantly in magnitude and ZFC curve shows a non-monotonic behaviour with a peak below Curie temperature. This can be explained by the ferromagnetic cluster model [81]. The hysteresis loop of the film displays a sharp increase in magnetization at low field (FM state), but there is no saturation at the high field due to the existence of AFM state (Figure 13(d)). However, the $R(T)$ curve for this sample shows semiconductive behaviour with a small gap.

For $x = 1$, the $M(T)$ curves in ZFC and FC modes show a canted antiferromagnetic behaviour, which has also been reported previously [64]. Based of these data, we can conclude that, for $x = 0.8$ sample with AFMI state below T_{N}, the C type AFM magnetic structure can be assumed. The $x = 0.9$ sample with exhibition of degenerate semiconductive behaviour the G type AFM structure with FM component can be considered, similar to observed for other low bandwidth manganites [82; 35; 9].

The CMR phenomenon was observed in both samples with $x = 0.8$ and $x = 0.9$, as already seen earlier in $Sm_xCa_{1-x}MnO_3$ [9] with the same concentrations. The magnetoresistivity properties are stronger at $x = 0.9$. To find any first order transition in these samples, their crystalline structure was investigated by XRD from 80 K to 450 K, but the samples did not show any change in crystalline structure at this temperature range. It supposed to the sample structure should be investigated at 10 K, where the magnetoresistance properties have been observed.

In conclusion, due to smaller $\langle r_A \rangle$ values (Table 4) , the T_{C} values obtained from

$M(T)$ curves for GCMO series in complete Ca doping range are smaller than those of SCMO and PCMO manganites. Similar to SCMO and PCMO, the ferromagnetic metallic state was not observed in GCMO family because of relatively small $\langle r_A \rangle$ and thus too narrow e_{g} electron bandwidth. As generally known, ferromagnetic metallic (FMM) state strongly depends on rare earth cation size, following a large bandwidth [12].

The phase diagram in figure 12 was defined from the magnetization and hysteresis curves (figure 13) and previous literature on other low bandwidth manganites, which suggests that the ground state of the mid-doping range is antiferromagnetic. However, after careful theoretical calculations [110] and the measurements on thin films [IV], it was suspected that the ground state could be ferromagnetic after all. To analyze the magnetic properties in more detail, the Curie-Weiss analysis was performed for all the Ca-dopings. Selected fits of the data to the Curie-Weiss law

$$\chi = \frac{C}{T - \theta_p} \tag{10}$$

are shown in figure 14 along with the obtained θ_{p} values for all samples. The intercept with the temperature axis, θ_{p} is observed to be positive for all samples. In the low x range ($0.0 < x \leq 0.3$), it is quite small and coincides well with the observed ferromagnetic transition temperature in [I]. In the mid x range ($0.4 \leq x \leq 0.7$)), where one would expect to have negative θ_{p} arising from the antiferromagnetic coupling, we actually observe an increase in θ_{p} in accordance with the theoretical calculations [110]. In high-doping range ($x \geq 0.8$) θ_{p} decreases again. In hindsight, it would have been beneficial to do this analysis already during the original analysis of the data. It should also be noted that the magnetic interactions in GCMO are very complicated and that the simple Curie-Weiss analysis does not give definite answers in this case. Changing of the ground state does not change any of the made conclusions as the charge-ordering is the more dominant phenomenon.

4.1.3 Magnetocaloric effect based on magnetic transition entropies

The magnetocaloric effect (MCE) depends on magnetic transition entropies. According to Eq. (3) in chapter 1, the temperature dependent magnetic state in materials can lead to change in entropy, ΔS, and consequently, refrigerator capacity, RC within the desired operating temperature range. The investigation of MCE in GCMO series [II] was motivated by observation of large RC values at low temperature in PCMO system [60]. The entropy change, ΔS, deduced from $M(T)$ curves in FC mode with applying external magnetic field in the range of 0.01–5 T and the magnetocaloric RC values of GCMO throughout the x range were presented in [II]. Here we just present RC values vs. Ca concentration in Figure 15 (a). In the hole doped region, although the largest ΔS was observed in sample with $x = 0.0$ due to large magnetic moments of Gd sublattice, the maximum RC was observed in $x = 0.1$ due to wider transition and the smaller magnetic coercivity. However, the temperature, where RC is at maximum is too low (T = 7 K) to be technologically significant. In the Mid-doped region associated with PM–CO transition near room temperature, the entropy change

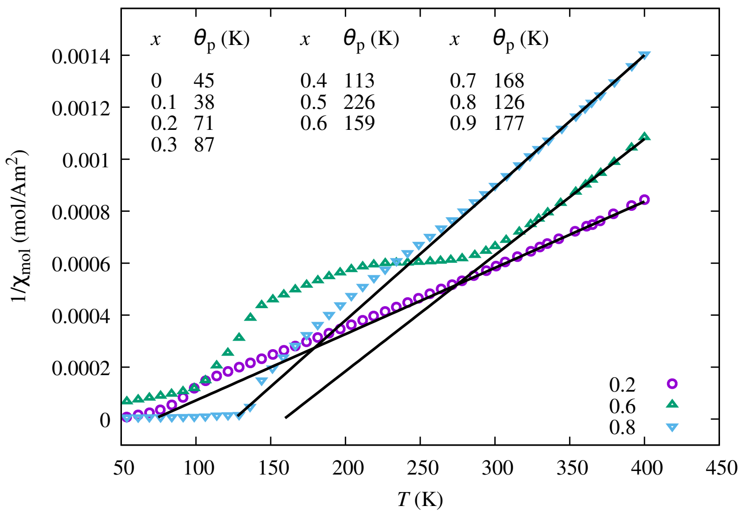

Figure 14. The inverse molar susceptibility of the $x = 0.2$, 0.6 and 0.8 samples with the Curie-Weiss fit the selected samples. All the fits were made at $T >$330 K. The θ_p values are given for all Ca-doping concentrations.

related to this and RC are impractically small. In the electron doped region, the entropy change obtained from strong PM-FM transition in sample with $x = 0.9$ is up to 19.9 JkgK^{-1}. Nonetheless, the transition is very sharp and too narrow to produce applicable RC. Figure 15(b) illustrates the $M(T)$ and ΔS curves for this sample.

4.2 GCMO thin films

4.2.1 The effect of substrate on structural properties

As expected, the deposition of thin films on different substrates usually results in distorted single crystalline materials, which can affect the physical properties of the films [83; 84; 85]. One common way to find the level of the distortion is comparison of the material lattice parameters to the substrate lattice parameters, which can be extracted by XRD technique. Moreover, the difference between the deposited material and the substrate lattice parameters affects the growth direction of the films. As reported earlier, the films grow in a direction, which minimizes the lattice mismatch between the film and the substrate. The mismatch can be evaluated by

$$M_\sigma = \frac{a_\mathrm{f} - a_\mathrm{s}}{a_\mathrm{f}}, \tag{11}$$

where a_f is the lattice parameter of the films and a_s is the diagonal of the substrate unit cell. For example, the smaller mismatch of GCMO lattice parameter and STO substrate is found in [110] direction (diagonal of STO unit cell) in the in-plane direction, leading to the growth of the [001] axis is the out-of-plane direction.

In this research, the XRD θ–2θ scans in $(00l)$ direction was done to find the lattice

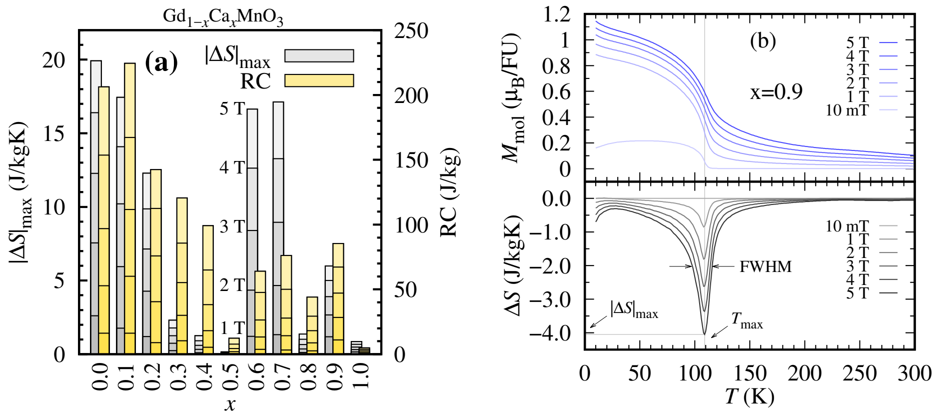

Figure 15. (a) The refrigerant capacities, RC, deduced from the maximum magnetic entropy changes, ΔS_{max} , and the ΔS_{max} values obtained from magnetic transitions for the complete Ca doping range. (b) The molar magnetizations and the entropy changes for sample with x = 0.9 [II].

parameters in the out-of-plane direction (c) and to determine the possible impurity phases (Figure 16(a-d)).

To find out the lattice parameters in the in-plane directions a and b, the θ–2θ measurements were implemented in $(0kk)$ and $(hh2h)$ directions. In addition, to explore the twin boundaries and grain boundaries, 2-dimensional $\phi - 2\theta$ scans of (224) peaks were carried out. After identifying the GCMO peak positions from the XRD patterns, GCMO lattice constants were calculated from the equation, which defines the relation between the Miller indices, (hkl), and the distance between the nearest plane in the real lattice space

$$\frac{1}{d} = \sqrt{\frac{h^2}{a^2} + \frac{k^2}{b^2} + \frac{l^2}{c^2}}. \tag{12}$$

The lattice parameters and microstructural properties depend on the lattice mismatch between GCMO and the substrate used in the deposition process through the structural stress, which causes elongation or compression of the unit cell of the films. When the first layer of atoms sits on the substrate, the lattice mismatch induces strain into the film in order to minimize the difference between the film and the substrate unit cell size. As we can find in previous literature, in a very thin film, the in-plane unit cell a film matches the substrate unit cell [86]. However, by increasing the film thickness, the effect of strain weakens and the lattice parameters relax towards the bulk values.

Due to lack of comprehensive studies about GCMO thin films and to find the optimal substrates for fabrication of high quality thin films, we deposited the GCMO films with selected concentration (x = 0.4) on $SrTiO_3$ (STO), $SrLaAlO_3$ (SLAO), $(LaAlO_3)_{0.3}(Sr_2AlTaO_6)_{0.7}$ (LSAT) and MgO substrates. The effect of lattice mismatch between the GCMO and the substrate on structural, magnetic and electrical properties was investigated in [III]. The lattice mismatches between the average of the GCMO bulk lattice parameters (a and b) and the diagonal of all substrate are listed in Table 3. The negative mismatch corresponds to expansive lattice stress in

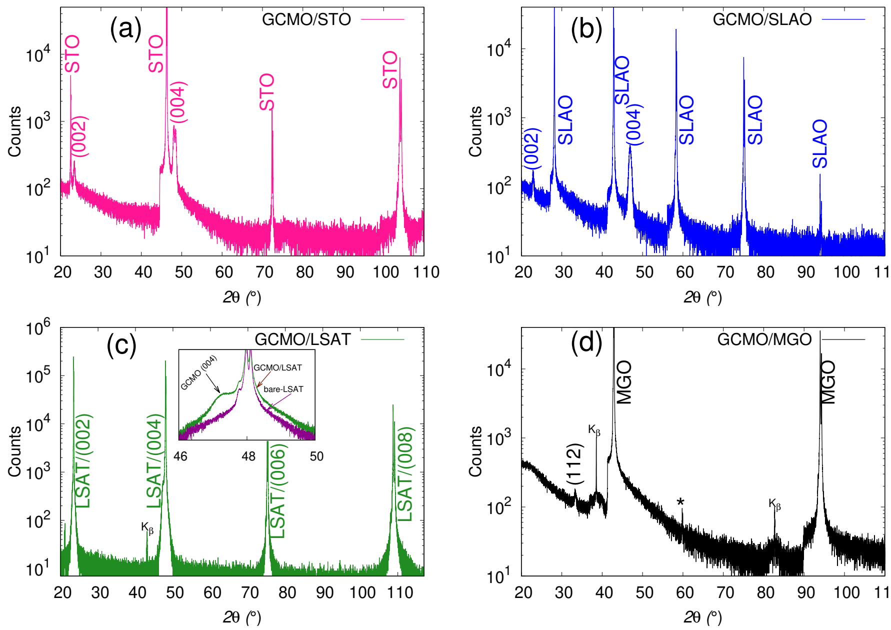

Figure 16. The $\theta - 2\theta$ XRD measurements in $(00l)$ direction for GCMO thin films deposited on substrates used in this work at room temperature. The asterisk (*) shows the unidentified peak, which can be arisen from the sample holder. The inset shows the (004) peak overlapped with the substrate peak compared with the bare substrate [III].

Table 3. Lattice parameters of the substrates and lattice mismatches between the diagonal of the substrate's unit cell and the average of the lattice parameters of GCMO bulk in the in-plane direction [III].

Substrate	a_s (Å)	c_s (Å)	f (%)
STO	3.905		+2.350
LSAT	3.868		+0.84
SLAO	3.756	12.636	-2.088
MGO	4.213		+9.847

Table 4. The GCMO lattice parameters, the substrate induced strain ε_a and ε_c along the in-plane and out-of-plane directions, respectively. The peak widths are determined from $\theta - 2\theta$ scan of (004) peak and $\phi - 2\theta$ scan of (224) peak. The values of the peak widths for the GCMO film grown on LSAT can not be determined due to the overlapping of GCMO peaks with the substrate peaks [III].

Substrate	a (Å)	b (Å)	c (Å)	ε_a (%)	ε_c (%)	$\Delta 2\theta(^\circ)$	$\Delta\phi(^\circ)$
STO	5.41(5)	5.46(3)	7.52(3)	0.2	0.03	0.68	2.7
SLAO	5.30(4)	5.30(2)	7.72(3)	-2.22	2.7	0.52	1.7
LSAT	5.34(1)	5.37(5)	7.61(4)	-1.08	1.2	–	–

the in-plane direction resulting in tensile strain, which again leads to the elongation of a and b parameters. The tensile strain leads to shrinkage of the out-of-plane lattice parameter, c.

As can be seen from the data in Table 3, the lattice mismatch between the GCMO and MgO substrate is the largest among the substrates. The XRD pattern of this film shows that the film is not textured but polycrystalline. The smallest lattice mismatch belongs to the GCMO grown on LSAT, and the peaks of GCMO film overlap with the substrate peak, as expected. To determine the lattice parameters of the GCMO film, we consider the substrate peaks as the film peaks in in-plane direction and the out-of-plane lattice parameters were calculated from the shoulder shown in Figure 16(c). However, this means that the information about the widths of the film peaks in the XRD pattern is impossible to obtain. The lattice parameters, the strain induced along a and c directions and the film peak widths are shown in Table 4. As expected from the lattice mismatch for the GCMO/SLAO film, the strain in the in-plane (ε_a) direction is compressive, consequently, this leads to elongation of unit cell along the c axis. On the STO film, the out-of-plane lattice parameter is expanded slightly with small magnitude strain even though the in-plane strain is tensile. We can say that the length of the c axis can be affected by the deposition parameters and structural defects in the films prepared by pulsed laser deposition method [87; 88].

In order to investigate the domain structure and dislocations at the interface between the GCMO film and the substrates, the cross-sectional HRTEM technique was used, as presented in [III]. As can be seen from the HRTEM images and the Fast

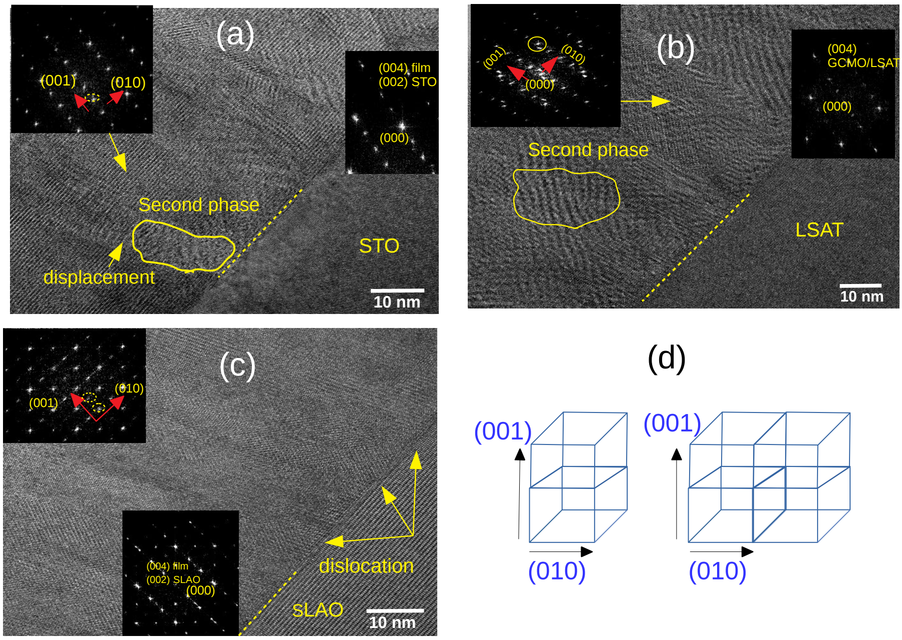

Figure 17. The cross-sectional HRTEM images along $\langle 100 \rangle$ direction of GCMO deposited on (a) STO, (b) LSAT and (c) SLAO substrates. The insets are diffraction patterns of the film (upper right corner) and the film-substrate interface (upper left corner). The dash-circle shows the reflections of the half integer peaks in the FFT images. The circle indicates the variation of the a/b axes in GCMO film grown on LSAT. (d) The illustration shows the unit cell doubling along out-of-plane direction (left) and along both in-plane and out-of-plane directions (right) [III].

Fourier Transform (FFT) of the images in Figure 17, the film on STO substrate shows half integer reflection in (001) direction, which means that the unit cell doubles is in this direction. It seems that the GCMO film grows on STO in the direction perpendicular to the film/substrate interface, leading to c oriented film. In addition, nanoclusters of a secondary phase has been recognized in this film. The impurity could be the oxygen deficient GCMO or MnO. However, the amount of the secondary phase is too small to observe it from the XRD patterns.

On GCMO/SLAO film, there is a sharp interface between the GCMO film and the substrate with dislocations starting from the interface, which can be due to compressive strain. The FFT image shows half integer reflections in both perpendicular and parallel directions to the interface between the GCMO film and the substrate. We can say that the doubling of the unit cell happened in both $\langle 010 \rangle$ and $\langle 001 \rangle$ directions, indicating multidomain microstructure in the film. In order to find mosaic domain microstructure in this film, a close view of the HRTEM was explored. The FFT image from the local region showed various diffraction patterns in this film. The two twinned domains (here labelled as A and B) with c axis along (001) and (010) directions, respectively, and the third domain (labelled C) with cb plane tilted 8 degrees clockwise from the (010) direction of the twin boundary were observed. This

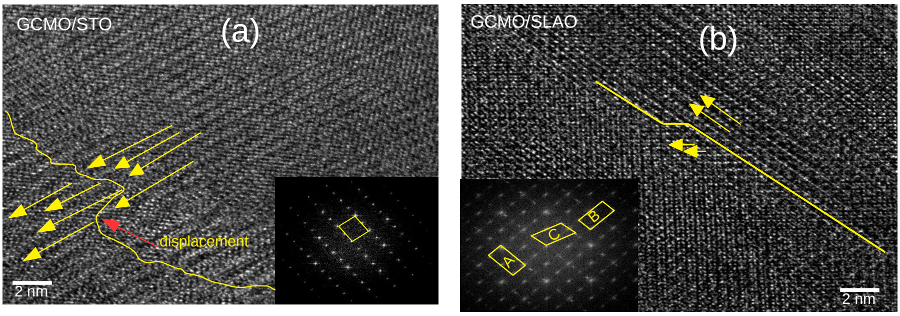

Figure 18. The planar-view TEM image of (a) GCMO/ STO and (b) GCMO/SLAO films. The domain walls and the domain orientation shown by solid lines and yellow arrows, respectively. The displacement in domain wall indicated by red arrow. The insets exhibit the FFT images of the GCMO films in order to show the unit cell orientation, which is displayed by parallelogram [III].

can be attributed to the mosaic domain microstructure.

The magnetic and resistivity properties were measured for the all films. The results were presented in [III] and shown schematically in Figure 19. To sum up, according to the measured data and HRTEM images, to have well crystallized and c oriented GCMO films, STO is the optimal substrate for these materials, even though a small secondary phase was observed. Therefore, in this study, we have concentrated on the physical properties of the GCMO films grown on STO substrate.

4.2.2 Structure of GCMO thin films (0$\leq x \leq$1)

The structural properties of the GCMO thin films with 0$\leq x \leq$1 were investigated by XRD technique and the results were presented in [IV]. The results showed that all the films are textured and well crystallized without any impurity phases. The calculated lattice parameters, lattice mismatches and FWHM values of the XRD peaks are given in [IV] and collected in Table 5. From the data, the FWHM values determined from θ-2θ measurements are below 1° for all the films, indicating uniform c parameter. With the knowledge of that the Ca ions are larger than Gd, however, the unit cell size of the GCMO decreases with increasing Ca concentration. This can be attributed to converting Mn^{3+} to Mn^{4+} by substitution of Ca in Gd atomic position. In the hole doped region (x$\leq$ 0.5), the calculated unit cell volume for GCMO thin films is larger when compared with that of GCMO bulk samples with the same Ca concentration. This is probably due to expansive lattice mismatch between the substrate and the films, which increases the length of the lattice parameters in the in-plane direction. In the electron doped region (x$\geq$ 0.5), the difference between the unit cell size of GCMO films and the bulk samples is insignificant despite of expansive lattice mismatch between the films and the substrate. We can say that the unit cell volume not only depends on film-substrate lattice mismatch but it can be affected by oxygen vacancies or oxgyen vacancy complexes.

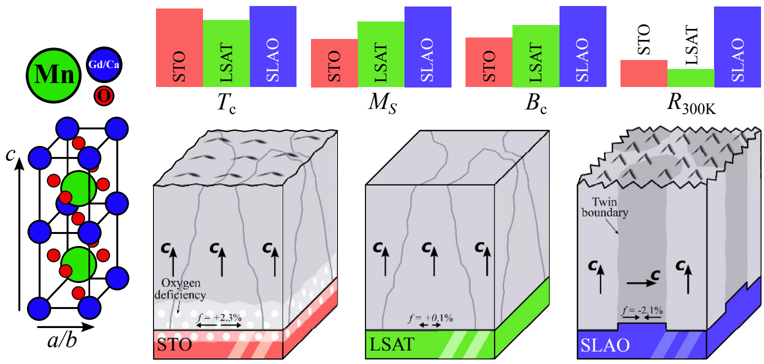

Figure 19. The illustration shows the domain orientations of the GCMO films grown on different substrates. The GCMO/STO and GCMO/LSAT films are c oriented in out-of-plane direction. The GCMO/SLAO has twinned domains with c axis oriented in out-of-plane and in-plane directions. The oxygen deficiency in the interface layer for GCMO/STO film is shown by white dots. The f is lattice mismatch between GCMO bulk and the substrates. The bars show the summary of magnetic properties and resistivity for the all films, T_C stands for Curie temperature, M_s for magnetization at 5 T, B_c for coercive field and R_{300} for resistivity at room temperature [III].

Table 5. The GCMO films on STO with varying Ca concentration are listed with structural results: The lattice parameters, M_a, M_b, V, 2θ FWHM, ϕ FWHM and d [IV].

x	a (Å)	b (Å)	c (Å)	M_a (%)	M_b (%)	V_{cell} (Å^3)	FWHM 2θ (°)	FWHM ϕ (°)	d (nm)
0.0	5.333	5.887	7.528	3.5	-6.2	236.344(1)	–	0.66	31
0.1	5.391(2)	5.88(3)	7.558(2)	2.8	-6.1	235.0997(4)	0.37	-	41
0.2	5.377(3)	5.872	7.531	2.7	-5.9	237.782(2)	0.39	0.91	46
0.3	5.372	5.503(2)	7.455(1)	2.8	0.35	220.385(5)	0.38	2.46	53
0.4	5.357	5.434	7.548(3)	3.1	1.6	219.722(2)	0.5	3.04	53
0.5	5.411	5.456(2)	7.417(4)	2	1.2	218.968(3)	0.31	1.27	55
0.6	5.345(4)	5.446(4)	7.400	3.3	1.4	215.406(4)	0.26	1.14	63
0.7	5.341	5.379(3)	7.396(1)	3.4	2.7	212.481(4)	0.3	1.40	68
0.8	5.319(3)	5.367(2)	7.386	3.8	2.9	210.849(4)	0.28	0.99	83
0.9	5.311(3)	5.341(4)	7.379(2)	4	3.4	209.313(1)	0.23	1.08	105
1.0	5.293(4)	5.284(1)	7.390(1)	4.3	4.5	206.685(2)	0.21	0.86	110

Table 6. The structural results extracted from XRD data for pristine and treated films with 0.4 and 0.9 Ca concentration listed with the lattice parameters, V, FWHM values from 2θ and ϕ scans [V], [VI].

x = 0.4	a (Å)	b (Å)	c (Å)	V_{cell} (%)	FWHM $2\theta(°)$	FWHM $\phi(°)$
Pristine	5.43	5.40	7.5	219.84	0.56	2.89
O_2-treated	5.38	5.40	7.5	218.06	0.51	2.7
Vacuum-treated	5.45	5.42	7.55	223.02	0.33	2.15
x = 0.9	a (Å)	b (Å)	c (Å)	V_{cell} (%)	FWHM $2\theta(°)$	FWHM $\phi(°)$
Pristine	5.30	5.28	7.45	208.65	0.26	2.16
O_2-treated	5.30	5.27	7.44	208.51	0.23	2.18
Vacuum-treated	5.41	5.29	7.48	214.01	0.46	7.18

4.2.3 Effect of annealings on crystallographic and electronic properties

The unit cell volume, V, for both GCMO films with x = 0.4 and x = 0.9 slightly decreases with oxygen treatment, while it increases with vacuum annealing in comparison with the pristine film. This can be attributed to the increased number of Mn^{3+} ions with ionic radius of 0.07 nm, when compared with the Mn^{4+} ions with ionic radius of 0.05 nm with vacuum annealing, leading to increased unit cell size. On the other hand, removing oxygen atoms with atomic radius of 0.12 nm from MnO_6 octahedron could lead to shrinkage of the unit cell. It seems that, in this set of GCMO films, the former one dominates and the vacuum treated sample with greater number of Mn^{3+} ions has larger unit cell, whereas the oxygen treated sample has smaller unit cell, when compared with the pristine sample.

For x = 0.4 sample, the determined peak widths (FWHM) in both 2θ and ϕ directions decrease in vacuum treated film, indicating lower variation in the lattice parameter in the c direction and smaller number of low-angle grain boundaries in comparison with the pristine film. In contrast for x = 0.9, the FWHM values show that the vacuum treatment induces large variation in both the in-plane and out-of-plane directions when compared with the pristine one. This was also confirmed with the 2D scan of (224) peak, which shows a clearly broadened peak in ϕ direction. This broadness can be a sign of twin boundaries, which come from structural disorder by inducing large amount of oxygen vacancies or oxygen vacancy complexes by vacuum annealing. All calculated lattice parameters, such as unit cell volume and FWHM values are presented in [V],[VI] and given in Table 6.

When the XRD data rely on diffraction from the crystal structure, another technique, x-ray photoelectron spectroscopy (XPS), which can define the oxidation state based on elemental binding energy. For manganites, with a knowledge that the physical properties mainly depend on Mn oxidation state, our XPS data analysis concentrates mainly on Mn ions.

The obtained full survey spectrum for pristine and treated samples for both concentrations, x = 0.4 and x = 0.9 shows that, in addition to Gd, Ca, Mn and O elements, there is a small peak of carbon contamination. Thus, all binding energy spectra of

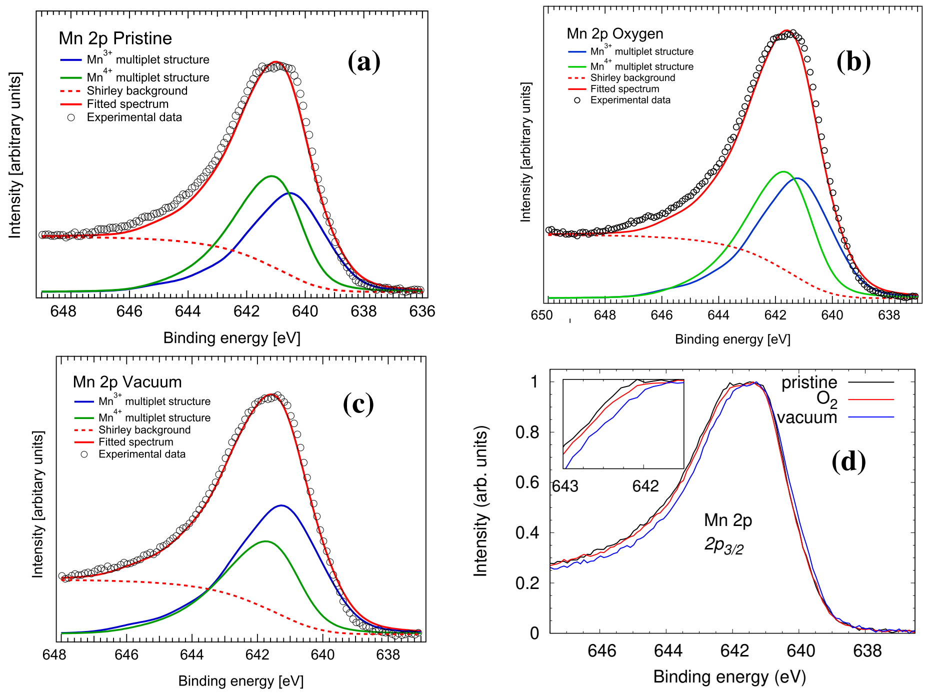

Figure 20. The XPS spectra of the Mn $2p_{3/2}$ core level with deconvelution results for the pristine and annealed samples x = 0.4 [V].

core levels were calibrated by C 1s binding energy to compensate the surface contamination. The broadness in the Mn 2p electronic state for both x = 0.4 and x = 0.9 indicates an overlap of Mn^{3+} $2p_{3/2}$ and Mn^{4+} $2p_{3/2}$ peaks, which can be attributed to coexistence of Mn^{3+} and Mn^{4+} ions [89; 90; 73]. For film with x = 0.4, the closer view of Mn $2p$ showed that the vacuum annealing results in narrower peaks, slightly shifting them to the lower binding energy in comparison with the pristine one, indicating a greater number of Mn^{3+} in this film. To confirm this, the spectra for pristine and treated films were fitted as shown by Biesinger et al [91] and the results are shown here (Figure 20) and in [V]. As can be seen from the fitting, the Mn^{3+}/Mn^{4+} ratio of vacuum GCMO is higher in comparison with pristine and oxygen treated samples.

For sample with x = 0.9, the Mn 2p peak shows a clear shift (0.96 eV) towards lower binding energy side after vacuum treatment, whereas the oxygen treatment causes a small shift towards higher binding energy side. As reported previously, these shifts can be attributed to the change of Mn^{3+}/Mn^{4+} ratio in the films [89; 90; 73]. The shift towards lower binding energy side stands for increase of Mn^{3+} ions and shift towards higher binding energy is due to increased number of Mn^{4+} ions. In addition, the Mn 3s core level spectra have been measured to confirm the change of Mn^{3+}/Mn^{4+} ratio with the annealings (Figure 21). The spectrum shows two peaks in different binding energy values due to the coupling of non-ionized 3s electron

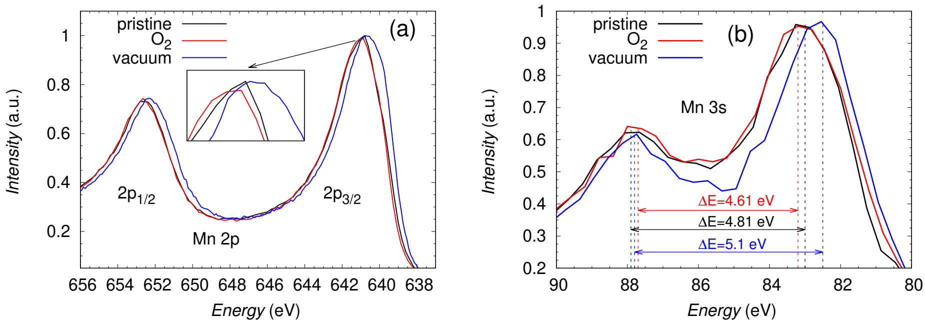

Figure 21. The XPS spectrum of Mn 2p and Mn 3s core levels with the magnitude of the splitting between 3s and 3d valence-band electrons of Mn ions for pristine and annealed films with x=0.9 [VI].

with 3d valence-band electrons [92]. The difference of the peaks position indicates the oxidation state of Mn, which means that ΔE for MnO (Mn^{2+}) is 6.0 eV, for Mn_2O_3 (Mn^{3+}) 5.3 eV and for MnO_2 (Mn^{4+}) 4.7 eV. In our films, for the pristine one ΔE is 4.81 eV, indicating mixture of Mn^{3+} and Mn^{4+} valences in the sample. This value increases to 5.1 eV, after vacuum annealing while it decreases to 4.6 eV in oxygen annealed film. Thus, we can say that the larger ΔE in the vacuum treated sample indicates the greater number of Mn^{3+} ions. Similarly, the opposite change, slightly decreased ΔE, can be due to the greater number of Mn^{4+} ions in the oxygen annealed sample when compared with the pristine one.

In this work, we can say that, although the oxygen treatment increases the number of Mn^{4+} ions slightly, the effect of vacuum treatment on structural and electronic properties is more significant in both Ca concentrations (x = 0.4 and 0.9) of GCMO.

4.2.4 Thickness analysis by XRR technique

To determine the thickness of the GCMO films, x-ray reflectivity measurements were done. The data were fitted by the GenX software [93] (Figure 22). From a four-layer model fitting, the thickness of the interface, GCMO films and the surface layer as well as roughness of the layers were obtained and are listed in Table 7. As reported previously, the interface layer between a film and a substrate is mostly dependent on lattice mismatch, oxygen vacancies and other defects [94; 98; 96]. On the other hand, Shimoyama *et al.* [97; 98] well explained that, when the RE compounds doped with $BaTiO_3$, $PbTiO_3$ or $SrTiO_3$ are epitaxially grown on STO substrate in low pressure of oxygen, the oxygen of the films is automatically fed from the substrate during the deposition. Therefore, we can say that in the case of GCMO films, the interface layer in the pristine samples can be due to lattice mismatch and oxygen vacancies induced by the substrate during the deposition process.

For x = 0.4 films, the thickness and the roughness of the interface layer decrease by oxygen treatment while they increase after vacuum annealing when compared to that of pristine film. It seems that the oxygen/vacuum annealing removes/introduces oxygen vacancies in this region, resulting in thinner/thicker and smoother/ rougher

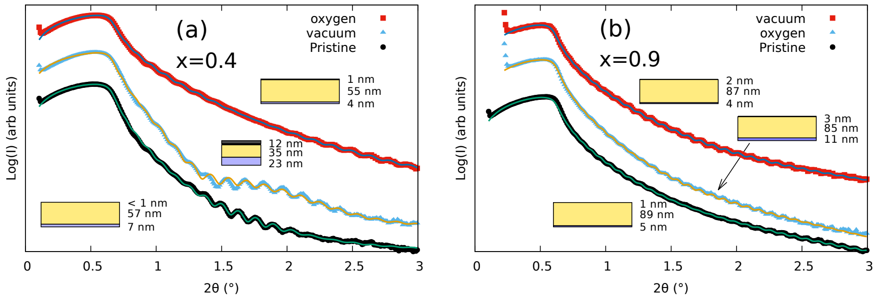

Figure 22. The room temperature experimental XRR data and fitted curves for pristine and treated GCMO films with x = 0.4 (a) and x = 0.9 (b) [V], [VI].

layer. The effect of oxygen and vacuum treatment on the film surface is similar to that of interface. This is in agreement with the previous literature [99; 100], which showed that film surfaces usually become thicker and rougher after vacuum treatment due to presence of higher concentration of oxygen vacancies.

For $x = 0.9$ films, the effect of vacuum and oxygen treatments on the roughness of the surface layer is insignificant, but the thickness of this layer increases only slightly (see Table 7). According to previous literature, introducing/removing oxygen vacancies in perovskites' lattice leading to thicker/thinner and rougher/smoother surface [99; 100]. In this set of films, even though the oxygen vacancies in the GCMO lattice can be filled by oxygen ions upon oxygen treatment, the film surface can also be oxidized. Thus, the surface roughness increases. In order to confirm this, the surface roughness of the all samples was measured by atomic force microscopy. The measurements showed that all the films have almost the same roughness, but density of the nanosized grains on the surface is higher for oxygen annealed film when compared with the pristine. It seems that the oxygen treatment increases the collisions among the evaporated atoms to reduce the kinetic energy, thus this lead to lowering surface diffusion of the adatoms, which favours the grain growth on the surface [101].

In the interface region, the oxygen annealing decreases the thickness while increases RMS roughness from 0.6 nm for pristine sample to 1.4 nm. This discrepancy can be explained by the reoxidization of substrate surface during the oxygen annealing process, which lead to TiO_2 double layer and Ti clusters on the substrate surface [111].

Generally, in this research we showed that the oxygen annealing can decrease the interface layer thickness in the GCMO thin films, although the process probably leads to rexidation of the substrate and induces higher amount of nanosized grains on the films' surface in comparison with the pristine samples. However, vacuum annealing increases the thickness of the interface and the surface layers in the GCMO thin films due to increasing number of oxygen vacancies in these regions.

Table 7. The thickness (D) and the roughness (r) of the GCMO films, surface and interface layer extracted from XRR fitting are presented for the pristine and treated films with x = 0.4 and x = 0.9. D_{inter} and r_{inter} stand for thickness and roughness of the interface, respectively. D_{surf} and r_{surf} are the thicknesses and roughnesses of the surface layers [V], [VI].

x = 0.4	D (nm)	D_{inter} (nm)	r_{inter} (nm)	D_{surf} (nm)	r_{surf} (nm)
Pristine	57	7	1	⟨1	2.8
O_2-treated	55	0.62	1	2	0.8
Vacuum-treated	35	23	3.5	12	3.7
x = 0.9	D (nm)	D_{inter} (nm)	r_{inter} (nm)	D_{surf} (nm)	r_{surf} (nm)
Pristine	89	5	0.6	1	0.5
O_2-treated	90	4	1.4	2	0.6
Vacuum-treated	88	11	3.8	3	0.6

4.2.5 Defect formation by positron annihilation spectroscopy

The concentration of open volume defects and oxygen vacancies in pristine and treated GCMO (x = 0.4 and 0.9) films were studied by positron annihilation spectroscopy (PAS) technique. In this technique, a positron beam is introduced into a sample and then, the positrons lose their kinetic energy due to delocalized lattice sites or vacancy like defects. The S parameter, which is the fraction of positrons annihilation with low momentum valence electrons and represents the type of vacancies and their concentration as a function of positron annihilation energy, E_{P}, is presented in Figure 23. The $S - E_{\mathrm{p}}$ curve illustrates the depth distribution of S, and hence, it changes with defect concentration across film thickness. The mean implantation depth of positron is shown by the upper horizontal axis. In both concentrations of GCMO films, the S values are constant above E_{P} = 6 keV, which means that almost all positrons reach the substrate and annihilate with bulk states.

The $S - E$ curves were fitted by the VEPFit code [102], which is used for multilayered systems to acquire thickness T, effective positron diffusion length L_{+}, and specific S-parameters for each layer within a stack. The fitting was done by assuming constant density and overall thickness for the films and the substrate. In this study, the density of GCMO films was theoretically calculated and the overall thickness of the GCMO films was determined from the XRR measurements. In GCMO case, two layers were considered for the fitting, i) sub-surface layer with relatively low defect concentration and ii) interface layer with greater number of open volume defects.

The calculated S, T, and L_{+} for both x = 0.4 and x = 0.9 films are listed in Table 8. In the interface region, vacuum treatment increases the thickness and decreases the diffusion length significantly for both Ca concentrations (x = 0.4 and x = 0.9). These indicate more defects in this region when compared with pristine film. Although the oxygen treatment decreases the thickness of the interface layer, it increases L_{+}. This means that the defect concentration increases in this region for both Ca concentra-

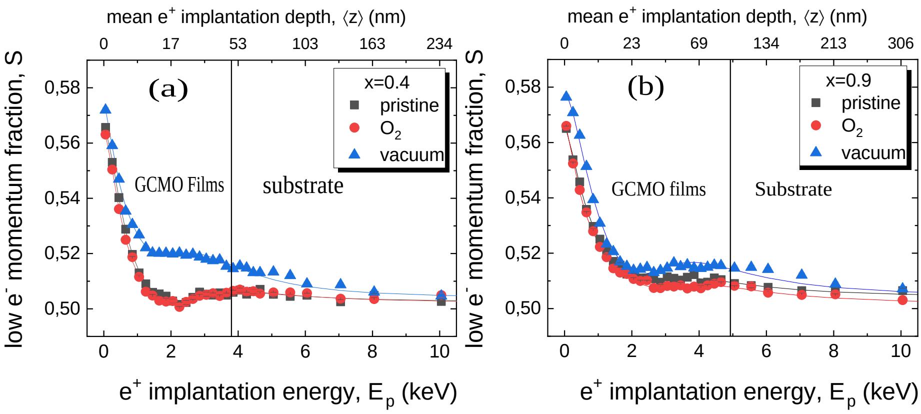

Figure 23. The S-E_p curves across the films thickness and the fitting results (solid curves) for (a) x = 0.4 and (b) x = 0.9 [V], [VI].

tions. These results are in agreement with the XRR data. In the sub-surface layer, L_+ increases/decreases by oxygen/vacuum annealing for film with x = 0.9. However, both vacuum and oxygen treatments increase L_+ value for samples with x = 0.4.

In order to understand the different defect types in GCMO films, lifetime positron annihilation measurements were done at room temperature. The measured lifetime spectrum was decomposed in two components τ_1 and τ_2. The values and their intensities are listed in Table 8. The short lifetime component, τ_1, stands for vacancy annihilation in B-site (V_B), which is a vacancy in the Mn site in the GCMO case. The longer component, τ_2, represents vacancies in A-site (V_A), indicating Gd or Ca vacancies in the GCMO samples. For GCMO films with 0.4 Ca concentration, τ_1 is 164–180 ps with 78 % intensity, which can be attributed to the vacancy in the Mn site or oxygen vacancy. The lifetime increases to 210 ps with 88 % intensity for vacuum annealed sample in both the film and substrate regions, which could be due to the formation of vacancy complex V_O–V_B in GCMO and the substrate. The τ_2 component is 300–320 ps with about 20 % intensity, for pristine sample. This is close to the lifetime values in the A-site vacancies (Gd or Ca vacancies in the GCMO case), but this value is somewhat larger than the theoretical value for A-site monovacancy [103; 104]. We can say that the obtained lifetime could be due to Gd or Ca vacancies or other open volume defects like grain boundaries. The intensity of τ_2 decreases by vacuum annealing. This is in agreement with XRR data. The effect of oxygen annealing on lifetime annihilation is insignificant. This could be due to the positively charged single oxygen vacancies, however, it cannot be directly shown with the PAS.

For x = 0.9, the lifetime positron annihilation results are similar to those of x = 0.4. However, the τ_2 value increases significantly after vacuum annealing. This could be due to existence of twin boundaries in this film, which is confirmed by the XRD measurements. In conclusion, the vacancy concentration in the A-site is a minority and the majority of the vacancy types are related to the oxygen vacancies or oxygen vacancy complexes with Mn vacancies in both Ca concentrations.

Table 8. The results of the positron lifetime studies are listed with S, T and L_+ parameters in subsurface and interface regions for differently treated GCMO thin films [V], [VI].

x = 0.4	S_1	T_1 (nm)	$L_{+,1}$ (nm)	S_2	T_2 (nm)	$L_{+,2}$ (nm)
Pristine	0.498(5)	43(1)	5.4(4)	0.517(1)	12	1
O_2-annealed	0.495(6)	43.4(9)	6.9(4)	0.521(1)	8.6	0.4
Vacuum-annealed	0.485(3)	25(1)	11.8(5)	0.539(3)	23	0.1–0.2
	$\tau 1$ (ps)	I_1 (%)	$\tau 2$ (ps)	I_2 (%)		
Pristine	185	78	320	22		
O_2-annealed	180	77	300	20		
Vacuum-annealed	210	88	360	10		
x = 0.9	S_1	T_1 (nm)	$L_{+,1}$ (nm)	S_2	T_2 (nm)	$L_{+,2}$ (nm)
Pristine	0.504	65(2)	10.7(4)	0.517(1)	25	0.6
O_2-annealed	0.502(6)	81(2)	17.7(5)	0.524(1)	9	0.5
Vacuum-annealed	0.494(3)	63(1)	7.1(5)	0.531(9)	27	0.1
	τ_1 (ps)	I_1 (%)	τ_2 (ps)	I_2 (%)		
Pristine	180	80	350	19		
O_2-annealed	180	80	300	18		
Vacuum-annealed	210	90	430	20		

4.2.6 Magnetic phase diagram of GCMO thin films

The magnetic phase diagram of the GCMO films as a function of Ca concentration and temperature was extracted from the temperature and field dependent magnetization measurements, which are shown in Figures 24(a)-(f).

In the hole doped region (0$\leq x \leq$0.3), where the GCMO lattice is highly distorted, the $M(T)$ curves for thin films are similar to those of bulk samples in the same Ca concentration. The curves show a maximum below the Curie temperature and the magnetization goes to the negative value at low temperature. This behaviour was explained in more detail for bulk samples in paper [I]. However, the hysteresis loops of the films show a metamagnetic transition, which was not observed in the bulk samples. This can be attributed to the lattice mismatch induced strain between the film and the substrate. The large lattice mismatch can induce more lattice distortion in the GCMO lattice, which can decrease the Mn–O–Mn bond angle. Thus, by applying external magnetic field, the magnetic moments of Mn atoms can easily rotate along the field.

In the mid-doped region (0.4$\leq x \leq$0.7), as expected from the previous publications, the existence of the OO/CO state at high temperature is the characteristics of the mixed low bandwidth manganites. In the GCMO case, the state was attributed to the observed hump at 360 K for the film with $x = 0.4$. In addition, the FC curve bifurcates ZFC curve at the same temperature for this film. As Ca increases, the bifurcation temperature increases to above 400 K in this region, while no hump was observed near room temperature for samples with 0.5$\leq x \leq$0.7. We can say that, the

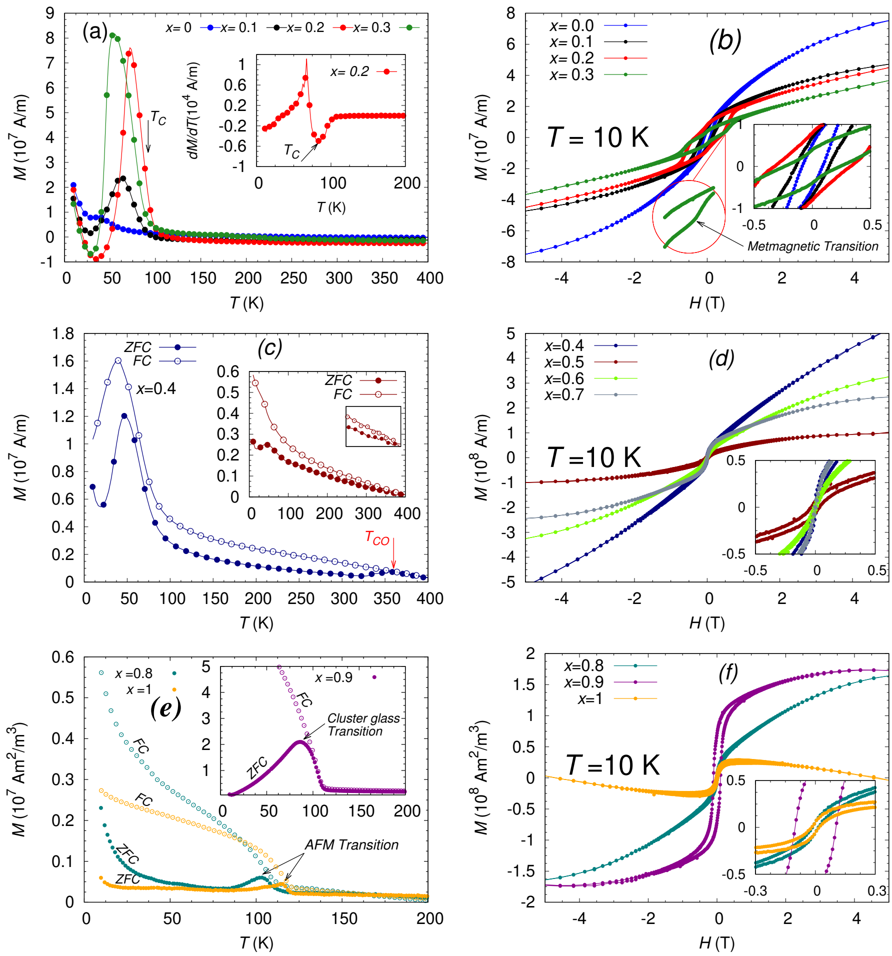

Figure 24. The temperature and field dependencies of magnetizations in GCMO films measured in low-doped region (a) and (b), mid-doped region (c) and (d), as well as in high-doped region (e) and (f) [IV].

OO/CO state probably occurs at temperatures higher than 400 K, where the bifurcation between ZFC and FC curves starts. Unfortunately, the $M(T)$ magnetization above 400 K cannot be measured with our facilities. In contrast, in the bulk samples the OO/CO state was initiated at x = 0.5 and, the state temperature is decreased with increasing Ca concentration [I].

The $M(H)$ measurements at 10 K for the films in this region show that in external magnetic field, the magnetization increases rapidly at low fields. This behaviour can be due to existence of FM phase. As the external field increases, the magnetization increases linearly with field and the magnetization does not saturate below 5 T. This behaviour stands for the AFM state in these films. According to the $M(T)$ and $M(H)$ data, it is suggested that there are FM clusters in the AFM long range OO/CO state in the background of the films in this Ca doping level. As can be seen from Figure 24(d), similar to the bulk sample, the film with x = 0.5 shows the smallest magnetization when compared with the other concentrations in this region. The possible explanation is the existence of stronger OO/CO state in this film.

In the electron doped region (0.8 $\geq$ x), the magnetization behaviour versus temperature and external magnetic field is quite similar to that of the bulk samples in this region. This means that in these Ca concentrations, there is coexistence of the FM phase coming from ferromagnetic double exchange interaction between Mn^{3+} – Mn^{4+} ions in the AFM matrix due to the antiferromagnetic superexchange interaction between Mn^{3+} – Mn^{3+} and Mn^{4+} – Mn^{4+}. We suggested that in the film of x = 0.8 with small peak below Curie temperature, the AFM interaction is dominated. This was confirmed with the $M(H)$ measurements, which do not show a FM regime as there is neither a sharp increase nor a saturation value of M with applied field.

As Ca concentration increases (x = 0.9), ZFC curve shows large hump and FC curve exhibits the significant increase in magnitude below the Curie temperature. It seems that the FM phase volume increases in this sample. The hysteresis loop of the film shows a sharp increase at low field. All these results indicate ferromagnetic behaviour. However, the hysteresis loop does not saturate up to 5 T. Thus, we can say that even though the volume of the FM phase increases in the film, a small fraction of AFM phase still exists. Moreover, the signature of training effect was observed in this film, which means that the virgin curve path is different than the subsequent cycles. In other words, the magnetization change is irreversible. This suggests that the applied external field induces a metastable FM phase in this film, attributing to cluster glass property, which is observed in the ZFC curve.

Figure 25 shows the determined magnetic phase digram based on $M(T)$ and $M(H)$ data of the GCMO thin films, which is similar to that of the GCMO bulk (see Figure 12). However, the magnetic ordering temperature (T_{C}, T_{N}) is slightly higher in thin films when compared with the bulk samples. The difference could be related to lattice mismatch and induced strain between the films and the substrate. As Millis et al. reported previously [105], the tensile strain leads to decreased T_{C}, while the compressive strain leads to increased T_{C} through the equation

$$T_{\mathrm{C}}(\varepsilon) = T_{\mathrm{C}}(\varepsilon = 0)(1 - \alpha\varepsilon_{\mathrm{B}} – 1/2\Delta\varepsilon^{*2}), \qquad (13)$$

where the ε_{B} and the ε^{*} are the uniform bulk strain and the JT strain, respectively. The $\alpha = (dT_{\mathrm{C}}/d\varepsilon_{\mathrm{B}})/T_{\mathrm{C}}$ and $\Delta = (dT_{\mathrm{C}}/d\varepsilon^{*})/T_{\mathrm{C}}$. The magnitude of α and Δ represents the relative weight of the symmetry-conserving bulk strain and the symmetry-breaking JT strain, respectively. The second term of Eq. (12) is connected to the

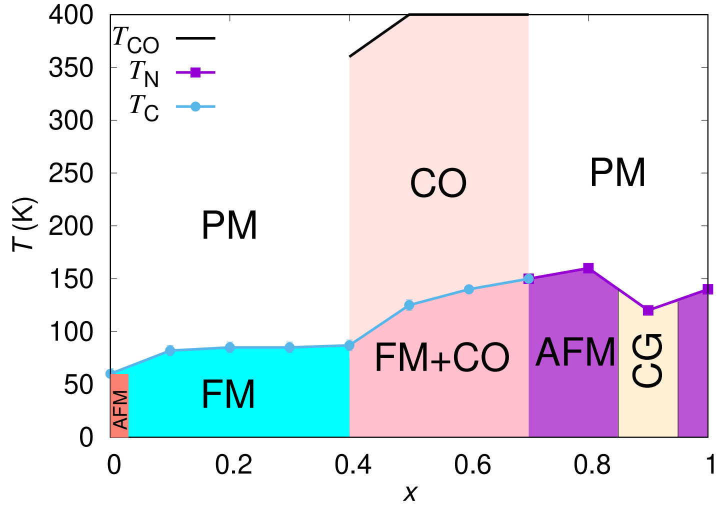

Figure 25. The magnetic phase diagram of GCMO films is extracted from magnetic measurements with T_{C}, T_{N} and T_{CO}. FM stands for ferromagnetic, AFM for antiferromagnetic, CG for cluster glass properties, CO for charge ordering and PM for paramagnetic [IV].

kinetic energy of the carriers, which can change with respect to the strain. This can be positive for tensile strain or negative for compressive strain. The third term of Eq. (12) corresponds to the electron localization due to the splitting of the e_{g} level caused by the static JT distortion. This is always negative in manganites. In GCMO, although the films are under tensile strain, the magnetic ordering temperature of the films is higher than that of bulk. It seems that the effect of structural disorder on T_{C} starts to dominate over the strain effect, leading to increased T_{C}.

4.2.7 Effect of annealing on magnetic and magnetoresistance properties

The effect of oxygen and vacuum treatment on magnetic properties and resistivity was also investigated. Temperature dependence of magnetization and resistance was measured in zero-field-cooled (ZFC) and field-cooled (FC) modes by applying an external magnetic field of 50 mT and 9 T, respectively, in the temperature range of 10–400 K.

For x = 0.4, as mentioned before, the GCMO films show a ferrimagnetic background due to large magnetic moment of Gd, which is oriented along the Mn ions in antiparallel direction (see section 4.1.2). As shown in Figure 26, the films exhibit a peak near Curie temperature. The maximum value of the peak decreases for vacuum treated sample in comparision with the pristine one. The maximum is attributed to ferromagnetic alignment of Mn ions in the direction of the applied field. The Mn ferromagnetic state can be explained by double exchange (DE) interaction, in which the Mn ions with different oxidation states interact with each other via oxygen atoms. By removing oxygen ions, the vacuum annealing process could suppress the DE interaction, consequently decreasing the magnetization and increasing the resistivity. However, the effect of vacuum treatment on Curie temperature is negligible. Introducing oxygen vacancies into the lattice of magnetic materials is expected to decrease the Curie temperature [106; 84; 105]. Thus, we can say that other factors such as low-angle grain boundaries and strain induced by the substrate can affect on Curie temperature. In this case, the vacuum treated film has the smallest lattice mismatch and the smallest number of grain boundaries among other films.

The temperature dependence of resistivity ($R(T)$) of pristine and annealed films are shown in Figure 26(b). For all the films, the resistivity increases gradually as temperature decreases, indicating insulating behaviour. The resistivity behaviour for the pristine and oxygen samples are similar, while the resistivity increases significantly by vacuum annealing treatment. The magnitude of resistivity at room temperature is given in [V] and in Figure 26(b). As reported earlier, in complex manganites, the transport properties are strongly affected by the oxygen concentration and structural disorder [107]. However, the oxygen concentration plays a key role in transport properties, when the films are slightly strained [108]. In other words, decreasing the oxygen content by vacuum annealing could lead to the increase in resistivity.

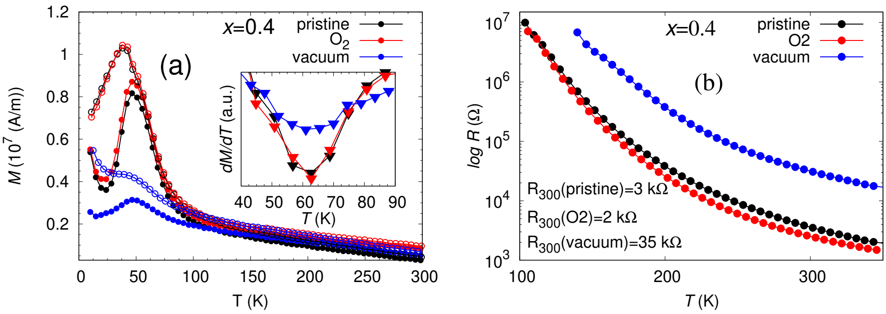

Figure 26. (a) The $M(T)$ curves in ZFC (filled symbols) and FC (open symbols) cycles measured in 50 mT for x=0.4. (b) The $R(T)$ curves of pristine and treated GCMO films. R_{300} is resistivity at room temperature. The data below 100 K is cut due to the large noise of the device [V].

From magnetic phase diagram of GCMO thin films, the samples belonging to the electron doped region show cluster glass properties, which means that there is coexistence of FM and AFM phase. This property is most significant in the sample with x = 0.9. In $M(T)$ curve, the FC magnetization increases significantly as temperature decreases and ZFC curve shows a peak below Curie temperature (Figure 27). It is assumed that this peak is due to cluster glass, which arises from the competition between FM phase arrested in the AFM matrix. The measured hysteresis loops presented in [VI], also confirm the coexistence of FM and AFM phases. As expected, adding oxygen to the GCMO lattice with 0.9 Ca concentration improves the DE interaction between Mn–O–Mn ions, resulting in larger magnetization and FM phase. In addition, the spin memory effect, which was reported for pristine sample previously [IV], was also observed in the oxygen treated film, being more significant with lower threshold field, 20 mT, in comparison with the pristine one (see Figure 27(b)).

The decrease of the threshold field for spin memory effect can be related to the increase of FM phase volume in the oxygen treated film. However, removing oxygen can destroy the DE interaction and cause frustration into the magnetic network that presumably could lead to spin glass magnetic state.

The Curie temperature decreases from 105 K for the pristine to 17 K for the vacuum annealed film, whereas the T_C increases slightly for oxygen treated film. Based on the previous study, oxygen vacancies and defects in the crystalline structure of manganites can lead to decreased magnetic ordering temperature [V]. In this case, the PAS results and XRD data show that the vacuum treated film has greater number of oxygen vacancies or oxygen vacancy complexes and also twin boundaries when compared with the pristine and oxygen annealed films. Thus, this could lead to decrease of T_C in the vacuum annealed film.

The temperature dependence of resistance, $R(T)$, was measured with 0 T and 9 T applied magnetic fields in a wide temperature range between 10–350 K. The pristine sample exhibits insulating-metal transition near 100 K (Fig. 26(c)), which could be attributed to existence of the FM phase in this film. One can expect that by increasing FM phase volume, the resistivity decreases. However, the resistivity increases after oxygen treatment, where the appearance of the $R(T)$ curve is similar to that of pristine one. The increased resistivity can be related to the local lattice distortions in the unit cell of GCMO film. Furthermore, as seen from the XRR and PAS results, the oxygen treated film has thicker dead layer at the surface with greater roughness and larger defect concentration at the interface when compared with the pristine film. It is suggested that the surface and interface can act as an insulating barrier due to the breakage of crystal symmetry of the film, resulting in weakening of electron hopping in the lattice. This can lead to increased resistance in this sample. The ZFC and FC curves are diverged below the metal-insulator transition. The separation is more noticeable in the oxygen treated sample in comparison with the pristine one, indicating stronger memory effect, which is in agreement with $M(H)$ measurements. The vacuum annealed film shows insulating behaviour, which is probably due to spin glass properties and lattice disorder in this sample.

Figure 27(d) displays the magnetoresistance property (CMR), extracted from $R(H)$ measurements at 10 and 50 K for pristine and oxygen samples. The curve at 10 K shows that the resistivity decreases as the magnetic field increases (path(1)), which means that the transition occurs from AFM-insulating (AFMI) state to FM-metallic (FMM) state. When the field is reversed, the resistivity changes in different path (2), and the films show smaller resistance at zero field compared to the virgin curve. One possible explanation is that the films recover to the original AFMI phase partially. This behaviour was reported also in [IX]. At 50 K, the difference between the virgin curve and the subsequent cycles of $R(H)$ curves decreases (see Figure 27(e)). This is probably due to thermal energy, which competes with the energy barriers between the FMM and AFMI phases, leading to weakened FMM phase. The difference between the resistivity of the subsequent cycle and virgin curves is larger in oxygen annealed film than in the pristine film, indicating larger non-volatile CMR property in this sample.

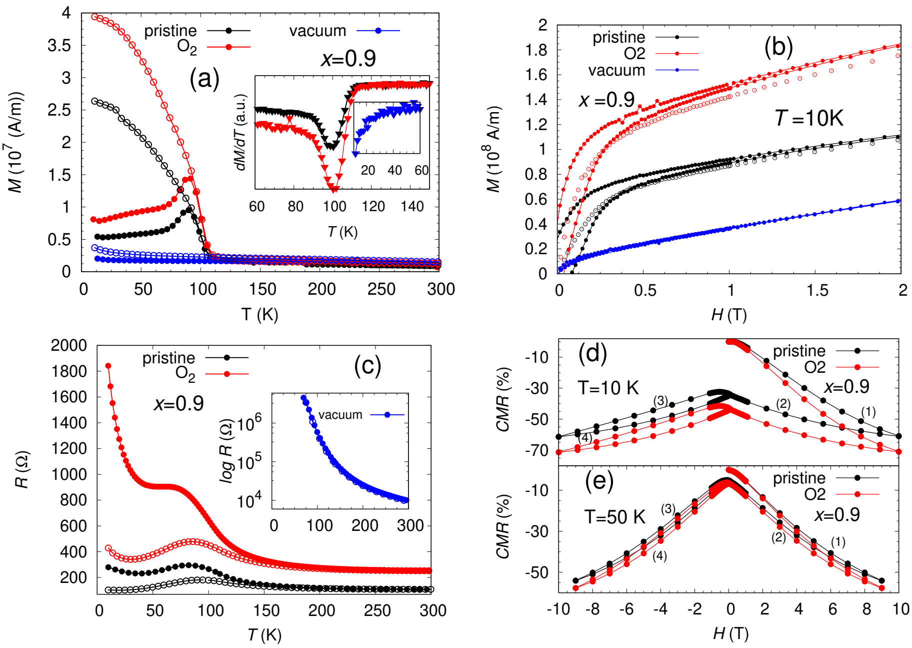

Figure 27. (a) The ZFC (filled symbols) and FC (open symbols) magnetization versus temperature curves measured in 50 mT field. The T_C is determined from the first derivative dM/dT of the FC magnetization, which is shown in the inset. (b) Part of the magnetic hysteresis loops together with virgin curves for pristine and for oxygen and vacuum treated films measured at 10 K indicating the memory effect in the pristine and oxygen annealed films. The hysteresis loops are given with filled symbols and the virgin curves with open circles. (c) Temperature dependences of the resistivities measured in 0 T (dots) and 9 T (open circles) fields for pristine as well as for oxygen and vacuum (inset) treated samples. (d) and (e) show the magnetic field dependence of the resistivity for pristine and oxygen annealed films measured at 10 and 50 K, respectively [VI].

5 Conclusions

The aim of this thesis is to do the base work in development of a novel memristor structure based on an electronic scale physical switching process for Gd-base manganites. Initially, the polycrystalline GCMO samples with varying Ca concentration (x = 0.0–1.0) were synthesized using the solid sate reaction method. The magnetic and electrical phase diagram of the samples, which was extracted based on magnetic and resistance measurements, showed different magnetic phases with increasing Ca doping level. The FMI state was characterized over hole concentration region (0$\leq x \leq$0.4). As Ca concentration increases, the CO-AFMI state for the range of 0.5$\leq x \leq$0.8 was observed. In the electron doped region ($x \geq$0.8) ferromagnetism with cluster glass properties appears and this is probably evidence of ferromagnetic components in a G type arrested in AFM state. In addition, the CMR properties have been observed for 0.8$\leq x \leq$0.9 samples. The GCMO manganites are structurally similar to PCMO, but the Gd cation has a smaller ionic radius than Pr, which entails a more distorted structure. This causes a lower bandwidth and more insulating bulk, which is beneficial in resistive switching applications due to lower leakage currents.

Due to the variety of magnetic transitions in the GCMO phase diagram, it was expected that the compounds can be a good candidate for magnetocaloric applications. The maximum refrigerator capacity (RC) was observed in $x = 0.1$ at T = 7 K due to wider transition and the smaller magnetic coercivity in comparison with other samples. In sample with $x = 0.9$, the strong PM-FM transition causes the large entropy change, however, the transition is very sharp and too narrow to produce applicable RC. Overall, it was found that GCMO is not a good candidate for magnetocaloric applications.

From the polycrystalline targets, the epitaxial GCMO thin films (x = 0.4) grown on different substrates showed that the lattice mismatch and strain can have a crucial role on structural, magnetic and electrical properties of the films. The GCMO film deposited on SLAO substrate with large compressive lattice mismatch exhibits domains with different orientation, leading to increase of coercive field and resistivity. On STO and LSAT, the films are c oriented, however, the structure on LSAT is more distorted due to negligible lattice mismatch. Both films contain a small amount of secondary phase, which can affect Curie temperature and magnetization.

The magnetic phase diagram was constructed for the full Ca doped concentrations set for GCMO thin films grown on STO substrate and compared with the phase diagram of the GCMO bulk samples. Similar to the bulk samples, in low-doped region, the ferromagnetic ordering of Mn ions, which are antiparallel with Gd ions at low temperature, were observed below Curie temperature. The OO/CO state and coexistence of FM and AFM phases were observed in mid-doped and high-doped regions, respectively. However, in comparison with the bulk samples, the OO/CO state were noticed in lower Ca concentration ($x \geq$ 0.4) above room temperature.

These results can be used to design a GCMO based memoristor device near room temperature as shown in [VIII]. In addition, GCMO thin films showed metamagnetic transition in the low-doped region, soft ferromagnetic behaviour in the mid-doped Ca concentration and memory effect in the electron doped region, which were not observed in the bulk samples.

At the end, the effect of oxygen content in GCMO thin films with Ca concentrations of x = 0.4 and x = 0.9 grown on STO substrate was investigated by *in situ* annealing in oxygen and vacuum atmospheres. In both concentrations, introducing more oxygen vacancies to the GCMO lattice, the double exchange interaction is suppressed, which leads to reduction in ferromagnetic coupling. This also increased resistivity, and in x = 0.9 case the ferromagnetic metallic pristine film transformed to antiferomagnetic insulator film after vacuum treatment. However, oxygen annealing increased magnetization and magnetoresistance properties slightly in the both Ca concentrations when compared with the pristine sample. For the GCMO films with x = 0.9, the memory effect was observed in lower magnetic field after oxygen treatment. The results were interpreted by a model suggested by the positron annihilation studies, where the concentration of oxygen vacancies and oxygen vacancy complexes in the A and B sites changes in both subsurface and interface regions by vacuum and oxygen annealings.

List of References

[1] A. Sawa. Resistive switching in transition metal oxides. *Materials Today*, 11:28, 2008.

[2] Anja Herpers, Christian Lenser, Chanwoo Park, Francesco Offi, Francesco Borgatti, Giancarlo Panaccione, Stephan Menzel, Rainer Waser, and Regina Dittmann. Spectroscopic proof of the correlation between redox-state and charge-carrier transport at the interface of resistively switching Ti/PCMO devices. *Advanced Materials*, 26:2730, 2014.

[3] A. Chen, J. Hutchby, V. Zhirnov, and G. Bourianoff. *Emerging Nanoelectronic Devices*. John Wiley and Sons Ltd, 2015.

[4] P. K. Siwach, H. K. Singh, and O. N. Srivastava. Low field magnetotransport in manganites. *J. Phys. Cond. Mat.*, 20:273207, 2008.

[5] L. Y. Kuai, Y. Y. Wei, and L. X. Guang. Colossal magnetoresistance in manganites and related prototype devices. *Chin. Phys. B*, 22:087502, 2013.

[6] M. Johnsson and P. Lemmens. *Crystallography and Chemistry of Perovskites. In Handbook of Magnetism and Advanced Magnetic Materials*. Wiely Online Library, 2007.

[7] Z. Zeng, M. Greenblatt, and M. Croft. Large magnetoresistance in antiferromagnetic $CaMnO_3$. *Phys. Rev. B*, 59:8784–8788, 1999.

[8] K. H. Ahn, T. Lookman, and A. R. Bishop. Strain-induced metal-insulator phase coexistence in perovskite manganites. *Nature*, 428:401, 2004.

[9] C. Martin, A. Maignan, M. Hervieu, and B. Raveau. Magnetic phase diagrams of $L_{1-x}A_xMnO_3$ manganites ($L =$ Pr,Sm; $A =$ Ca Sr). *Phys. Rev. B*, 60:12191–12199, 1999.

[10] J. P. Zhou, J. T. McDevitt, J. S. Zhou, H. Q. Yin, J. B Goodenough, Y. Gim, and Q. X. Jia. Effect of tolerance factor and local distortion on magnetic properties of the perovskite manganites. *Appl. Phys. Lett.*, 75:1146, 1999.

[11] V.M. Goldschmidt. Die gesetze der krystallochemie. *Naturwissenschaften*, 14:477–485, 1926.

[12] H. Y. Hwang, S. W. Cheong, P. G. Radaelli, M. Marezio, and B. Batlogg. Lattice effects on the magnetoresistance in doped $LaMnO_3$. *Phys. Rev. Lett.*, 75:914–917, 1995.

[13] H. A. Jahn and E. Teller. Stability of polyatomic molecules in degenerate electronic states. *Proc. R. Soc. A*, 161:220–235, 1937.

[14] M. D. Coey, M. Viret, L. Ranno, and K. Ounadjela. Electron localization in mixed-valence manganites. *Phys. Rev. Lett.*, 75:3910, 1995.

[15] P. Beaud, A. Caviezel, S. O. Mariager, L. Rettig, G. Ingold, C. Dornes, S.-W. Huang, J. A. Johnson, M. Radovic, T. Huber, T. Kubacka, A. Ferrer, H. T. Lemke, M. Chollet, D. Zhu, J. M. Glownia, M. Sikorski, A. Robert, H. Wadati, M. Nakamura, M. Kawasaki, Y. Tokura, S. L. Johnson, and U. Staub. A time-dependent order parameter for ultrafast photoinduced phase transitions. *Nature Materials*, 13:923, 2014.

[16] A. Dagotto, T. Hotta, and A. Moreo. Colossal magnetoresistant materials: the key role of phase separation. *Physics Reports*, 344:1, 2001.

[17] J.B Goodenough and L. Loeb. Theory of ionic ordering, crystal distortion, and magnetic exchange due to covalent forces in spinels. *Phys. Rev.*, 98:391, 1955.

[18] J. Kanamori. Crystal distortion in magnetic compounds. *J. Appl. Phys.*, 31:S14–S23, 1960.

[19] J. Kanamori. Superexchange interaction and symmetry properties of electron orbitals. *J. Phys. Chem. Solids*, 10:87, 1959.

[20] J. B. Goodenough. Theory of the role of covalence in the perovskite-type manganites (La,MII)MnO_3. *Phys. Rev.*, 100:564–573, 1955.

[21] P.W. Anderson. New approach to the theory of superexchange interactions. *Phys. Rev.*, 115:2, 1959.

[22] C. Zener. Interaction between the d-shells in the transition metals. ii. ferromagnetic compounds of manganese with perovskite structure. *Physical Review*, 81:440, 1951.

[23] Y. Tokura. *Colossal magnetoresistive oxides*. Gordon and Breach Science, New York, 2000.

[24] P. W. Anderson and H. Hasegawa. Considerations on double exhange. *Physical Review*, 100: 675, 1955.

[25] M. B. Salamon and M. Jaime. The physics of manganites: Structure and transport. *Rev. Mod. Phys*, 73:583, 2001.

[26] M. Imada, A. Fujimori, and Y. Tokura. Metal-insulator transitions. *Rev. Mod. Phys.*, 70:1039, 1998.

[27] Y. Tokura. Critical features of colossal magnetoresistive manganites. *Rep. Prog. Phys.*, 69: 797–851, 2006.

[28] A. J. Millis, P. B. Littlewood, and B. I. Shraiman. Double exchange alone does not explain the resistivity of $La_{1-x}Sr_xMnO_3$. *Phys. Rev. Lett.*, 74:5144, 1995.

[29] T. V. Ramakrishnan, H. R. Krishnamurthy, S. R. Hassan, and G. Venketeswara Pai. Theory of insulator metal transition and colossal magnetoresistance in doped manganites. *Phys. Rev. Lett.*, 92:157203–1, 2004.

[30] Z. Jirak, S. Krupicka, Z. Simsa, M. Dlouha, and S. Vratislav. Neutron diffraction study of PrCaMnO perovskites. *J. Magn. and Magn. Mater.*, 53:153, 1985.

[31] W. C. Koehler, H. L Yakel, E. O. Wollan, and J. W. Cable. A note on the magnetic structures of rare earth manganese oxides. *Phys. Lett.*, 9:93, 1964.

[32] S. M. Dunaevski. Magnetic phase diagrams of manganites in the electron doping region. *Physics of the Solid State*, 46:193–212, 2004.

[33] L. E. Gontchar, A. E. Nikiforov, and S. E. Popov. Interplay between orbital, charge and magnetic orderings in $r_{1-x}a_x mno_3$ (x = 0, 0.5). *J. Magn. and Magn. Mater.*, 223:175, 2001.

[34] L. E. Gontchar and A. E. Nikiforov. Superexchange interaction in insulating manganites $R_{1-x}A_xMnO_3$ (x=0, 0.5). *Phys. Rev. B*, 66:014437, 2002.

[35] H. Kawano, R. Kajimoto, H. Yoshizawa, Y. Tomioka, H. Kuwahara, and Y. Tokura. Magnetic ordering and relation to the metal-insulator transition in $Pr_{1-x}Sr_xMnO_3$ and $Nd_{1-x}Sr_xMnO_3$ with $x = 2$. *Phys. Rev. Lett.*, 78:4253–4256, 1997.

[36] Y. Tomioka, A. Asamitsu, H. Kuwahara, Y. Moritomo, and Y. Tokura. Magnetic-field-induced metal-insulator phenomena in $Pr_{1-x}Ca_xMnO_3$ with controlled charge-ordering instability. *Phys. Rev. B*, 53:R1689, 1996.

[37] Y. Tomioka, A. Asamitsu, Y. Moritomo, H. Kuwahara, and Y.Tokura. Collapse of a charge-ordered state under a magnetic field in $pr_{1/2}sr_{1/2}mno_3$. *Phys. Rev. Lett.*, 74:5108, 1995.

[38] A. Asamitsu, Y. Tomioka, H. Kuwahara, and Y. Tokura. Current switching of resistive states in magnetoresistive manganites. *Nature*, 388:50, 1997.

[39] H. Kuwahara, Y. Tomioka, A. Asamitsu, Y. Moritomo, and Y. Tokura. A first-order phase transition induced by a magnetic field. *Science*, 270:961, 1995.

[40] M. R. Lees, J. Barratt, G. Balakrishnan, and D. McK. Paul. Neutron-powder-diffraction study of the magnetic and structural properties of $Pr_{0.6}(Ca_{1-x}Sr_x)_{0.4}MnO_3$ $(0 \leq x \leq 1)$. *Phys. Rev. B*, 58:8694, 1997.

[41] Y. Tokura and Y. Tomioka. Colossal magneotresistive manganites. *J. Magn. and Magn. Mater.*, 200:1, 1999.

[42] K. F. Wang, Y. Wang, L. F. Wang, and S. Dong. Cluster-glass state in manganites induced by A-site cation-size disorder. *Phys. Rev. B*, 73:134411, 2006.

[43] Lide M. Rodriguez-Martinez and J. Paul Attfield. Cation disorder and size effects in magnetoresistive manganese oxide perovskites. *Phys. Rev. B*, 54, 1996.

[44] O. Chmaissem, B. Dabrowski, S. Kolesnik, J. Mais, J. D. Jorgensen, and S. short. Structural and magnetic phase diagram of $La_{1-x}Sr_xMnO_3$ and $Pr_{1-y}Sr_yMnO_3$. *Phys. Rev. B*, 67:094431, 2003.

[45] S. Kundu and T. K. Nath. Evidence of electronic phase arrest and glassy ferromagnetic behaviour in $(Nd_{0.4}Gd_{0.3})Sr_{0.3}MnO_3$ manganite: comparative study between bulk and nanometric samples. *J. Phys. Cond. Mat.*, 23:356001, 2011.

[46] A.I. Kurbakov. Electronic, structural and magnetic phase diagram of $Sm_{1-x}Sr_xMnO_3$ manganites. *J. Magn. and Magn. Mater.*, 322:967–972, 2010.

[47] P. Schiffer, A. P. Ramirez, W. Bao, and S-W. Cheong. Low temperature magnetoresistance and the magnetic phase diagram of $La_{1-x}Ca_xMnO_3$. *Phys. Rev. Lett.*, 75:3336, 1995.

[48] W. Prellier, Ph. Lecoeur, and B. Mercey. Colossal-magnetoresistive manganite thin films. *J. Phys. Cond. Mat.*, 13:R915, 2001.

[49] A. Beiranvand, J. Tikkanen, H. Huhtinen, and P. Paturi. Electronic and magnetic phase diagram of polycrystalline $Gd_{1-x}Ca_xMnO_3$ manganites. *J. Alloy Compd.*, 720:126–130, 2017.

[50] Michele Kotiugaa, Zh. Zhangb, J. Lic, F. Rodolakisd, H. Zhoud, and Ronny Sutarto. Carrier localization in perovskite nickelates from oxygen vacancies. *PNAS*, 116(44):21992–21997, 2019.

[51] W. Lu, P. Yang, W. D. Song, G. M. Chow, and J. Sh. Chen. Control of oxygen octahedral rotations and physical properties in $SrRuO_3$ films. *Phys. Rev. B*, 88:214115, 2013.

[52] S. Majumdar, H. Huhtinen, S. Granroth, and P. Paturi. Evolution of structural and magnetic properties with varying oxygen content in low-bandwidth manganite $Pr_{0.9}Ca_{0.1}MnO_3$ thin films. *J. Phys. Cond. Mat.*, 24:206002:1–8, 2012.

[53] V. Franco, J. Blázquez, B. Ingale, and A. Conde, The magnetocaloric effect and magnetic refrigeration near room temperature: Materials and models. *Annu. Rev. Mater. Res.*, 42:305–342, 2012.

[54] M.-H. Phan, S.-B. Tian, S. C. Yu, and A. N. Ulyanov. Magnetic and magnetocaloric properties of $La_{0.7}Ca_{0.3-x}Ba_xMnO_3$ compounds. *J. Magn. and Magn. Mater.*, 256:306, 2003.

[55] E. Brück, Developments in magnetocaloric refrigeration. *J. Phys. D: Appl. Phys.*, 38:R381, 2005.

[56] K. A. Gschneidner Jr, V. K. Pecharsky, and A. O. Tsokol, Recent developments in magnetocaloric materials. *Reports on Progress in Physics*, 68:1479, 2005.

[57] J. R. Gómez, R. F. Garcia, A. D. M. Catoira, and M. R. Gómez, Magnetocaloric effect: A review of the thermodynamic cycles in magnetic refrigeration. *Renewable and Sustainable Energy Reviews*, 17:74 – 82, 2013.

[58] P. Z. Si, D. Li, C. J. Choi, Y. B. Li, D. Y. Geng, and Z. D. Zhang. Large coercivityand small exchange bias in Mn_3O_4/MnO nanoparticles. *Solid State Communications*, 142:723, 2007.

[59] E. Pollert, S. Krupicka, and E. Kuzmicova. Structural study of $pr_{1-x}ca_xmno_3$ and $y_{1-x}ca_xmno_3$ perovskites. *J. Phys. Chem. Solids*, 43:1137, 1982.

[60] J. Tikkanen, H. Huhtinen, and P. Paturi. Oxygen-sintered $(Pr,Ca)MnO_3$: structure and magnetism at high Ca concentrations. *J. Alloys Comp.*, 635:41, 2015.

[61] L. Lutterotti, M. Bortolotti, G. Ischia, I. Lonardelli, and HR. Wenk. Rietveld texture analysis from diffraction images. *Z. Kristallogr. Suppl*, 26:125–130, 2007.

[62] D. B. Chrisey and G. K. Hubler. *Pulsed Laser Deposition of Thin Films*. John Wiley Sons Inc., 1994.

[63] T. Elovaara, T. Ahlqvist, S. Majumdar, H. Huhtinen, and P. Paturi. Melting of the charge-ordered state under substantially lower magnetic field in structurally improved $Pr_{1-x}Ca_xMnO_3$ (x = 0.3 - 0.5) thin films. *J. Magn. and Magn. Mater.*, 381:194, 2015.

[64] C. L. Flint, A. J. Grutter, C. A. Jenkins, E. Arenholz, and Y. Suzuki. Magnetism in $CaMnO_3$ thin films. *J. Appl. Phys.*, 115:17D712, 2014.

[65] M. McCormack, S. Jin, T. H. Tiefel, R. M. Fleming, and Julia M. Phillips. Very large magnetoresistance in perovskite like La-Ca-Mn-O thin films. *J. Appl. Phys.*, 64:3045, 1994.

[66] P. Paturi, J. Tikkanen, and H. Huhtinen. Room temperature charge-ordered phase in $Gd_{0.6}Ca_{0.4}MnO_3$ and $Sm_{0.6}Ca_{0.4}MnO_3$ thin films. *J. Magn. Magn. Mater.*, 432:164 –168, 2017.

[67] J. Als-Nielsen and D. McMorrow. *Elements of modern x-ray physics*. Wiley, 2010.

[68] H. Zabel. X-ray and neutron reflectivity analysis of thin films and superlattices. *Appl. Phys. A Solids Surfaces*, 58:159–168, 1994.

[69] E. Chason and T. M. Mayer. Thin film and surface characterization by specular x-ray reflectivity. *Critical Reviews in Solid Sttite und Materials Sciences*, 22(1):1–61, 1997.

[70] M. Yasaka. X-ray thin-film measurement techniques. *The Rigaku Journal*, 26(2):1–9, 2010.

[71] H. Kiessig. xrr measurents. *Ann. phys.*, 10:715–768, 1931.

[72] P. Van der Heide. *X-ray photoelectron spectroscopy : an introduction to principles and practices*. Wiley, 2012.

[73] E. Beyreuther, S. Grafström, L. M. Eng, C. Thiele, and K. Dörr. XPS investigation of Mn valence in lanthanum manganite thin films under variation of oxygen content. *Phys. Rev. B*, 73: 155425:1–9, 2006.

[74] R. D. Shannon. Revised effective ionic radii and systematic studies of interatomic distances in halides and chalcogenides. *Acta Crystallographica Section A*, 32:751, 1976.

[75] A. Kurbakov. Electronic, structural and magnetic phase diagram of $Sm_{1-x}Sr_xMnO_3$ manganites. *J. Magn. and Magn. Mater.*, 322:967–972, 2010.

[76] Y. Martin and H. K. Wickramasinghe. Magnetic imaging by "force microscopy" with 1000 Å resolution. *Appl. Phys. Lett.*, 50:1455, 1987.

[77] Z. Jirak, S. Vratislav, and J. Zajicek. The magnetic structure of $Pr_{0.9}Ca_{0.1}MnO_3$. *Phys. Stat. Sol. A*, 52:K39, 1979.

[78] A. Maignan, C. Martin, F. Damay, and B. Raveau. Complex competition between ferromagnetism and antiferromagnetism in the CMR manganites $Pr_{1-x}Ca_xMnO_3$. *Z. Phys. B*, 104:21, 1997.

[79] M. Uehara, S. Mori, C. H. Chen, and S.-W. Cheong. Structural changes, clustering, and photoinduced phase segregation in $Pr_{0.7}Ca_{0.3}MnO_3$. *Nature*, 399:560–563, 1999.

[80] M-H. Jo, N. D. Mathur, N. K. Todd, and M. G. Blamire. Very large magnetoresistance and coherent switching in half-metallic manganite tunnel junctions. *Phys. Rev. B*, 61:R14905, 2000.

[81] H. Nam, K. Jonason, P. Nordblad, N. V. Khiem, and N. X. Phuc. Coexistence of ferromagnetic and glassy behavior in the $La_{0.5}Sr_{0.5}CoO_3$ perovskite compound. *Phys. Rev. B*, 59:4189, 1999.

[82] A. Maignan, C. Martin, F. Damay, and B. Raveau. Factors governing the magnetoresistance properties of the electron-doped manganites $Ca_{1-x}A_xMnO_3$ (A = Ln, Th). *J. Chem. Mater.*, 10: 950–954, 1998.

[83] R. A. Rao, D. Lavric, T. K. Nath, and C. B. Eom. Three-dimensional strain states and crystallographic domain structures of epitaxial colossal magnetoresistive $La_{0.8}Ca_{0.2}MnO_3$ thin films. *Appl. Phys. Lett.*, 73:3294–3296, 1998.

[84] Y. P. Lee and S. Y. Park. Lattice-strain-driven ferromagnetic ordering in $La_{0.8}Sr_{0.2}MnO_3$ thin films. *Appl. Phys. Lett.*, 84:777–779, 2004.

[85] F. Jin, M. Gu, C. Ma, Er-J. Guo, J. Zhu, L. Qu, Z. Zhang, K. Zhang, L. Xu, B. Chen, F. Chen, G. Gao, J. M. Rondinelli, and W. Wu. Uniaxial strain–controlled ground states in manganite films. *J. Nano Lett.*, 20:1131–1140, 2020.

[86] W. Prellier, Ch. Simon, A. M. Haghiri-Gosnet, B. Mercey, and B. Raveau. Thickness dependence of the stability of the charge-ordered state in $Pr_{0.5}$ $Ca_{0.5}$ MnO_3thin films. *Phys. Rev. B*, 62: R16337–R16340, 2000.

[87] D. O. Klenov, W. Donner, B. Foran, and S. Stemmer. Impact of stress on oxygen vacancy ordering in epitaxial $(La_{0.5}Sr_{0.5})CoO_{3-a}$thin films. *Appl. Phys. Lett.*, 82:3427–3429, 2003.

[88] G. V. Bazuev, A. P. Tyutyunnik, A. V. Korolev, E. Suard, C. W. Tai, and N. V. Tarakina. The effect of manganese oxidation state on antiferromagnetic order in $SrMn_{1-x}Sb_xO_3$ ($0\leq x \leq 0.5$) perovskite solid solutions. *J. Mater. Chem. C*, 7:2085–2095, 2019.

[89] H. Felhi, M. Smari, A. Bajorek, K. Nouri, E. Dhahri, and L. Bessais. Controllable synthesis, XPS investigation and magnetic property of multiferroic $BiMn_2O_5$ system: The role of neodyme doping. *Prog. Nat. Sci.*, 29:198–209, 2019.

[90] J. Gao, S. Y. Dai, and T. K. Li. Electronic states epitaxial thin films of $La_{0.9}Sn_{0.1}MnO_3$ and $La_{0.9}Ca_{0.1}MnO_3$. *Phys. Rev. B*, 67:153403:1–4, 2003.

[91] M. C. Biesinger, B. P. Payne, A. P. Grosvenor, L. W. M. Lau, A. R. Gerson, and R. C. Smart. Resolving surface chemical states in xps analysis of first row transition metals, oxides and hydroxides: Cr, Mn, Fe, Co and Ni. *Applied Surface Science*, 257:2717–2730, 2011.

[92] V. R. Galakhov, S. Bartkowski M. Demeter, M. Neumann, N. A. Ovechkina, E. Z. Kurmaev, N. I. Lobachevskaya, Ya. M. Mukovskii, J. Mitchell, and D. L. Ederer. Mn 3s exchange splitting in mixed-valence manganites. *Phys. Rev. B*, 65:13102, 2002.

[93] M. Björck and G. Andersson. Genx: an extensible x-ray reflectivity refinement program utilizing differential evolution. *J. Appl. Cryst.*, 40:1174–1178, 2007.

[94] R. Herger, P. R, Willmott, C. Schleputz, M. Bjorck M, S. A. Pauli, D. Martoccia and B. D. Patterson Structure determination of monolayer-by-monolayer grown $La_{1x}Sr_xMnO_3$ thin films and the onset of magnetoresistance. *Phys. Rev. B.*, 77:085401:1–10, 2008.

[95] K. Shimoyama, M. Kiyohara, A. Uedono and K. Yamabe Epitaxial growth of $BaTiO_3$/$SrTiO_3$ structures on SrTiO3 substrate with automatic feeding of oxygen from the substrate. *Jpn. J. Appl. Phys.*, 41:L269, 2002.

[96] A. Uedono, K. Shimayama, M. Kiyohara, Z. Q. Chen and K. Yamabe Study of oxygen vacancies in $SrTiO_3$ by positron annihilation. *J. Appl. Phys.*, 92:2697–2702, 2002.

[97] K. Shimoyama, K. Kubo, T. Maeda, and K. Yamabe. Epitaxial growth of $BaTiO_3$ thin film on $SrTiO_3$ substrate in ultra high vacuum without introducing oxidant. *Jpn. J. Appl. Phys.*, 40:L463, 2001.

[98] K. Shimoyama, M. Kiyohara, A. Uedono, and K. Yamabe. Homoepitaxial growth of $SrTiO_3$ in an ultrahigh vacuum with automatic feeding of oxygen from the substrate at temperatures as low as 370 c. *Jpn. J. Appl. Phys.*, 41:L269, 2002.

[99] F. Li, Y. Zhan, T. H. Lee, X. Liu, A. Chikamatsu, T. Guo, H. J. Lin, J. C. A. Huang, and M. Fahlman. Modified surface electronic and magnetic properties of $La_{0.6}Sr_{0.4}MnO_3$ thin films for spintronics applications. *J. Phys. Chem. C*, 115:16947–16953, 2011.

[100] C. Wang, K. j. Jin, L. Gu, H. b. Lu, S. m. Li, and W. j. Zhou. Crucial role played by interface and oxygen content in magnetic properties of ultrathin manganite films. *Appl. Phys. Lett.*, 102: 252401:1–4, 2013.

[101] M. Ohring. *Materials Science of Thin Films (Second Edition)*. Academic Press, 2002.

[102] A. van Veen, H. Schut, M. Clement, J. M. M. de Nijs, A. Kruseman, and M. R. Ijpma. VEPFIT applied to depth profiling problems. *Appl. Surf. Sci.*, 85:216–224, 1995.

[103] R. A. Mackie, S. Singh, J. Laverock, S. B. Dugdale, and D. J. Keeble. Vacancy defect positron lifetimes in strontium titanate. *Phys. Rev. B*, 79:014102:1–8, 2009.

[104] V. J. Ghosh, B. Nielsen, and T. Friessnegg. Identifying open-volume defects in doped and undoped perovskite-type $LaCoO_3$, $PbTiO_3$, and $BaTiO_3$. *Phys. Rev. B*, 61:207–212, 1999.

[105] A. J. Millis, T. Darling, and A. Migliori. Quantifying strain dependence in colossal magnetoresistance manganites. *J. Appl. Phys.*, 83:1588–1591, 1998.

[106] S. V. Trukhanov, I. O. Troyanchuk, and F. P. Korshunov. Effect of oxygen content on magnetization and magnetoresistance properties of CMR manganites. *J. Low Temp. Phys.*, 27:283–287, 2001.

[107] M. Salvato, A. Vecchione, A. De Santis, F. Bobba, and A. M. Cucolo. Metal-insulator transition temperature enhancement in $La_{0.7}Ca_{0.3}MnO_3$ thin films. *J. Appl. Phys.*, 97:103712:1–5, 2005.

[108] B. Li, L. Yang, J. Z. Tian, X. P. Wang, H. Zhu, and T. Endo. Influence of compressive strain on oxygen distribution in $La_{0.7}Ba_{0.3}MnO_3$ thin films. *J. Appl. Phys.*, 109:073922:1–5, 2011.

[109] A. Beiranvand, M. O. Liedke, C. Haalisto, V. L. ahteenlahti, A. Schulman, S. Granroth, H. Palonen, M. Butterling, A. Wagner, H. Huhtinen, and P. Paturi. Tuned AFM-FM coupling by the formation of vacancy complex in $Gd_{0.6}Ca_{0.4}MnO_3$ thin film lattice. *J. Phys. Cond. Mat.*, 33: 255803, 2021.

[110] H. Ben Hamed, M. Hoffmann, W. A. Adeagbo, A. Ernst, W. Hergert, T. Hynninen, K. Kokko, and P. Paturi. First-principles investigations of the magnetic phase diagram of $Gd_{1-x}Ca_xMnO_3$. *PHYSICAL REVIEW B*, 99:144428, 2019.

[111] R. Herger, P. R. Willmott, O. Bunk, C. M. Schleputz, B. D. Patterson and B. Delley. Surface of Strontium Titanate. *Phys. Rev. Lett.*, 98:076102, 2007.

TURUN YLIOPISTO
UNIVERSITY OF TURKU

Painosalama Oy, Turku, Finland 2022

ISBN 978-951-29-8864-8 (PRINT)
ISBN 978-951-29-8865-5 (PDF)
ISSN 0082-7002 (Print)
ISSN 2343-3175 (Online)